JEM Journal of Experimental Medicine

ARTICLE

Qki is an essential regulator of microglial phagocytosis in demyelination

Jiangong Ren[1*], Congxin Dai[1,2*], Xin Zhou[1,3*], Joseph A. Barnes[1,4], Xi Chen[1], Yunfei Wang[5], Liang Yuan[1,6], Takashi Shingu[1], Amy B. Heimberger[7], Yiwen Chen[8], and Jian Hu[1,4]

The mechanism underpinning the regulation of microglial phagocytosis in demyelinating diseases is unclear. Here, we showed that the Quaking protein (Qki) in microglia was greatly induced by demyelination in the brains of both mice and humans. Deletion of the Quaking gene (*Qk*) in microglia severely impaired the clearance of myelin debris. Transcriptomic profiling indicated that depletion of Qki impaired total RNA levels and splicing of the genes involved in phagosome formation and maturation. RNA immunoprecipitation (RIP) confirmed the physical interactions between the Qki protein and the mRNAs of Qki targets that are involved in phagocytosis, indicating that Qki regulates their RNA stability. Both Qki depletion and inhibition of Qki target Cd36 greatly reduced the phagocytic activity of microglia and macrophages. The defective uptake and degradation of myelin debris caused by Qki depletion in microglia resulted in unresolved myelin debris that impaired axon integrity, oligodendrocyte maturation, and subsequent remyelination. Thus, our results demonstrate that Qki is an essential regulator of microglia's phagocytic activity under demyelinating conditions.

Introduction

Microglia, the unique resident immune cells in the central nervous system (CNS), not only play a pivotal role in maintaining the homeostasis of a normal brain but also participate in the frontline defense against neurological diseases, including demyelinating diseases (Lenz and Nelson, 2018; Sarlus and Heneka, 2017; Wake et al., 2011). In response to pathological conditions, microglia rapidly activate, proliferate, and migrate to the lesions (Colonna and Butovsky, 2017; Fu et al., 2014). The role of activated microglia in influencing pathological outcomes is twofold: the first is to clean up damaged tissues by phagocytosing cell debris, and the second is to help tissues regenerate by secreting cytokines, chemokines, and growth factors (Fu et al., 2014; Li and Barres, 2018). However, whether microglia have beneficial or deleterious functions in demyelinating diseases is still a matter of debate (Gao and Tsirka, 2011; Muzio et al., 2007; Neumann et al., 2009). On the one hand, microglia have been suggested as a damaging element in neurodegenerative diseases due to inappropriate activation of their phagocytic activity (Aguzzi et al., 2013). Depletion or inactivation of microglia delayed symptom onset and alleviated the severity of clinical symptoms in an experimental autoimmune encephalomyelitis (EAE) model (Bhasin et al., 2007; Gao and Tsirka, 2011; Heppner et al., 2005). Additionally, microglia could act as antigen-presenting cells (which also depend on their phagocytic activity), leading to T cell activation and numerical expansion, which are known to aggravate disease progression (Gao and Tsirka, 2011; Luo et al., 2017). On the other hand, microglia might also play beneficial roles in demyelinating diseases by removing apoptotic cells and myelin debris through phagocytosis, which paves the way for the maturation of oligodendrocyte progenitor cells (OPCs) and subsequent tissue regeneration (Lampron et al., 2015; Natrajan et al., 2015; Neumann et al., 2009). For instance, decrease in the phagocytic activity of microglia in both humans and mice has been shown to delay recovery from demyelinating conditions (Janda et al., 2018; Linehan et al., 2014; Poliani et al., 2015). Therefore, these seemingly contradictory functions of microglia in demyelinating diseases indicate that the phagocytic activities of microglia are contextually dependent on the types and stages of demyelinating lesions.

Despite the fact that microglia are the primary phagocytes in the CNS, little is known about the molecular mechanisms underpinning the regulation of phagocytosis in microglia. Thus,

[1]Department of Cancer Biology, The University of Texas MD Anderson Cancer Center, Houston, TX; [2]Department of Neurosurgery, Beijing Tongren Hospital, Capital Medical University, Beijing, China; [3]Cancer Research Institute of Jilin University, The First Hospital of Jilin University, Changchun, Jilin, China; [4]The University of Texas MD Anderson Cancer Center UT Health Graduate School of Biomedical Sciences, Houston, TX; [5]Department of Melanoma Medical Oncology, The University of Texas MD Anderson Cancer Center, Houston, TX; [6]Graduate School of Biomedical Sciences, Tufts University, Boston, MA; [7]Department of Neurosurgery, The University of Texas MD Anderson Cancer Center, Houston, TX; [8]Department of Bioinformatics and Computational Biology, The University of Texas MD Anderson Cancer Center, Houston, TX.

*J. Ren, C. Dai, and X. Zhou contributed equally to this paper; Correspondence to Jian Hu: jhu3@mdanderson.org.

deciphering the regulatory mechanisms of phagocytosis under different conditions may dampen the deleterious actions of microglia yet stimulate their phagocytic activity that is specific for debris removal, which could lead to amelioration of clinical outcomes of demyelinating diseases.

Phagocytosis is a specialized form of endocytosis by which phagocytes engulf solid particles from the extracellular space (Rosales and Uribe-Querol, 2017; Uribe-Querol and Rosales, 2017). Microorganisms, dying cells, and cell debris can all be targets of phagocytosis (Arandjelovic and Ravichandran, 2015; Underhill and Goodridge, 2012). Once internalized, the engulfed particles are packaged within a special type of endosome–phagosome, which then fuses with the lysosome for degradation (Underhill and Goodridge, 2012). Phagocytosis is a highly coordinated process and is divided into four major steps: (1) recognition of the target particles, (2) activation of the internalization machinery, (3) phagosome formation, and (4) phagolysosome maturation (Rosales and Uribe-Querol, 2017; Uribe-Querol and Rosales, 2017). However, understanding of the major regulators of the phagocytic process, particularly in response to various stress conditions, is rather limited. The Mitf/Tfeb/Tfe3 family of transcription factors has been implicated in regulating phagocytosis, but these transcription factors mainly regulate the formation and activity of lysosomes, which participate in the last stage of phagocytosis, phagolysosome maturation (Sardiello et al., 2009; Settembre et al., 2013). Therefore, efforts are needed for detailed understanding of the regulation of phagocytosis, especially the essential regulators and regulatory mechanism of phagocytosis under different pathological conditions.

Quaking (Qki) is a signal transduction and activation of RNA–family RNA-binding protein. It is involved in various aspects of RNA homeostasis, including RNA stability, splicing, and translation; microRNA processing; and circular RNA biogenesis (Chen et al., 2012; Conn et al., 2015; Darbelli and Richard, 2016; Hu et al., 2013). Other than its canonical function as an RNA-binding protein during oligodendrocyte differentiation and myelination (Chénard and Richard, 2008; Larocque et al., 2002; Li et al., 2000; Sidman et al., 1964), we recently reported that Qki-5 also works as a transcriptional coactivator of the PPARβ–RXRα complex to regulate the transcription of genes involved in fatty acid metabolism during myelin homeostasis (Zhou et al., 2020). Importantly, aberrant Qki expression is associated with multiple human diseases, such as schizophrenia, cancer, restenosis, and inflammatory diseases (Åberg et al., 2006; Chen et al., 2012, 2007; Conn et al., 2015; Darbelli and Richard, 2016; de Bruin et al., 2016; Hu et al., 2013; Shingu et al., 2017). Although there have been no reports on the role of Qki in microglia to date, Qki has been found to be involved in the differentiation of monocytes into macrophages (de Bruin et al., 2016; Fu et al., 2012; Wang et al., 2015). Intriguingly, studies on the functions of Qki in monocyte differentiation have given rise to controversial results. Two studies reported that Qki inhibited the differentiation of monocytes into macrophages (Fu et al., 2012; Wang et al., 2015), whereas another study showed that Qki promoted this process (de Bruin et al., 2016), indicating that the role of Qki in monocytes/macrophages might be context dependent. Our previous work with neural stem cells and glioma stem cells demonstrated that Qki is an important regulator of endolysosome-dependent member receptor degradation (Shingu et al., 2017). The important role of Qki in regulating endolysosomes in glioma prompted us to investigate the role of Qki in regulating phagocytosis in microglia. Since microglial phagocytosis is instrumental in modulating the brain's responses to demyelinating conditions (Prinz and Priller, 2014), we hypothesized that Qki regulates phagocytosis in microglia and plays a critical role in demyelinating diseases.

In this study, using a recently created murine model of *Qk* conditional knockout in our laboratory, we took advantage of a well-established cuprizone (CPZ)-induced demyelinating condition to investigate the role of Qki in microglia in response to demyelination. We found that the expression of Qki in microglia was dramatically induced by demyelination. The defective phagocytosis induced by depletion of Qki in microglia significantly impaired myelin debris clearance and eventually compromised remyelination. These results indicate that Qki is an essential regulator of phagocytosis in microglia in the context of demyelinating conditions.

Results

Qki in microglia is induced by demyelination in the CNS

To determine the functions of Qki in microglia in response to demyelination in the CNS, we selected the murine model of demyelination, in which oligodendrocytes are specifically killed by CPZ to induce demyelination (Matsushima and Morell, 2001; Praet et al., 2014). Consistent with previous studies (Gudi et al., 2014; Praet et al., 2014), mice treated with dietary CPZ for 4 wk developed demyelination in the corpus callosum (CC) with an associated accumulation of myelin debris (Fig. S1 A, right panels). CPZ-induced demyelination has also been reported to induce activation of microglia, but not the infiltration of bone marrow–derived myeloid cells (Kondo et al., 1987; Mildner et al., 2007). Since mice bearing *Cx3cr1*$^{CreER\text{-}EYFP}$ allele specifically express enhanced YFP (EYFP) in microglia (Parkhurst et al., 2013), which was confirmed by almost 100% concordance with Iba1 staining in the brain (Fig. S1 B), in this study, we used EYFP to mark Iba1$^+$ microglia. Microgliosis, which was indicated by hyperproliferation of EYFP$^+$ microglia, was found to be prominent in the demyelinating lesions of these mice (Fig. S1 B), suggesting that the CPZ-treated mouse is a reliable model of demyelination with great activation of microglia, allowing us to study Qki's function in microglia during demyelination. Up-regulation of phagocytic activity is one of the most consistent responses of microglia in coping with various stresses in the CNS, including demyelination. Therefore, we sought to determine whether Qki protein in microglia could be altered in response to CPZ-induced demyelination. Within EYFP$^+$ microglia cells, Qki protein levels were 5.9-fold higher in the 4-wk CPZ-induced demyelinating lesions than the levels of Qki in microglia in control mice fed a regular diet (Fig. 1, A and B), indicating that the Qki protein is induced by demyelination.

Next, we sought to rule out the possibility that the induction of Qki in microglia of CPZ-treated mice was due to the direct

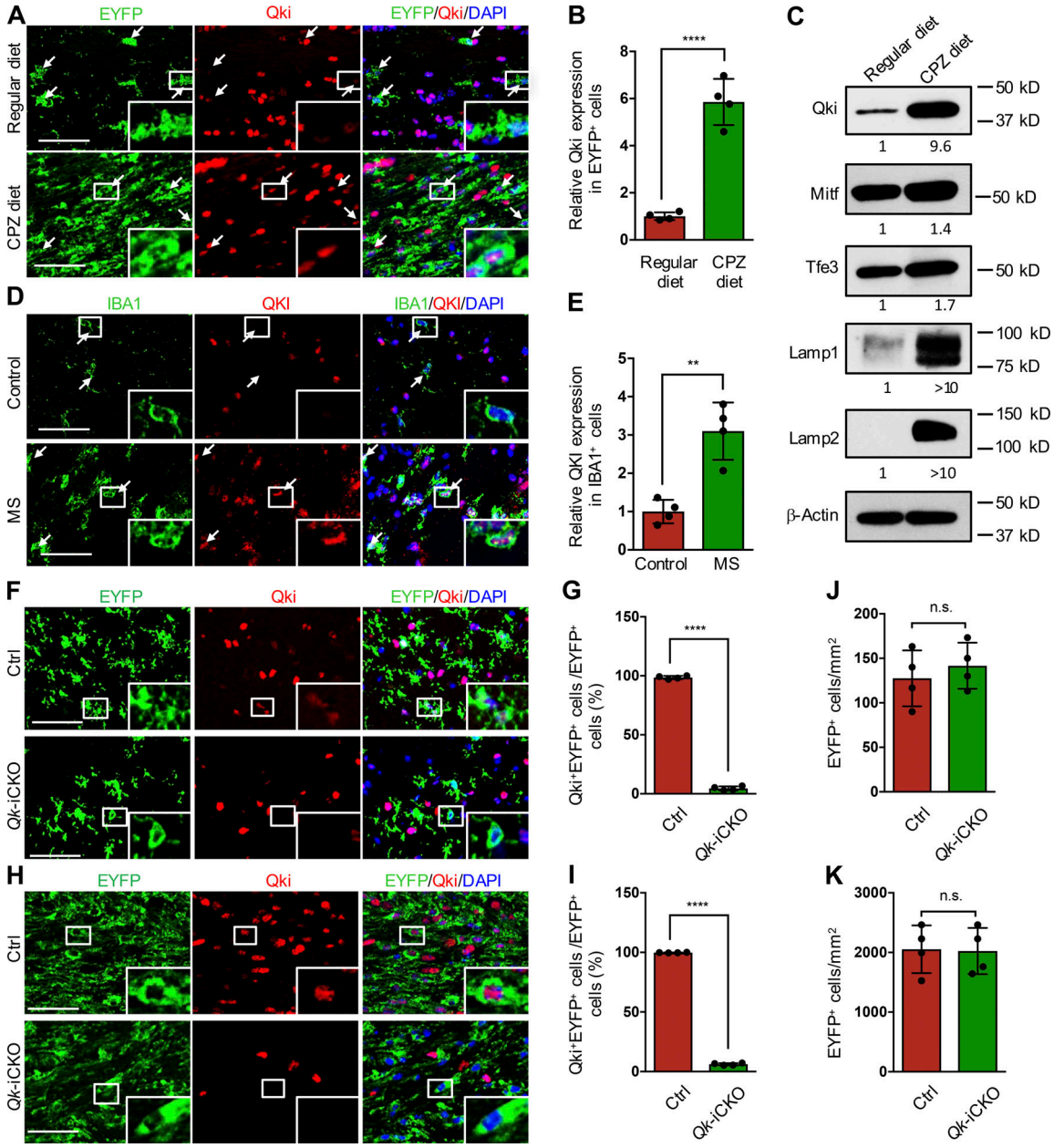

Figure 1. **Qki in microglia is induced by demyelination in the CNS, and depletion of Qki does not impair microgliosis in response to CPZ-induced demyelination. (A and B)** Representative images of IF and quantification of Qki and EYFP in the CC of 8-wk-old control mice fed the regular diet or the CPZ diet for 4 wk (n = 4 mice/group). **(C)** Western blotting showing the expression of Qki, the phagolysosomal components, and the regulators of phagocytosis in freshly isolated microglia from the CCs of 8-wk-old control mice fed the regular diet or the CPZ diet for 4 wk. The relative expression of these proteins was normalized with the loading control of β-actin. Data represent three independent experiments. **(D and E)** Representative images of IF and quantification of QKI and IBA1 in the lesions of patients with MS and the white matter of normal brain (n = 4 samples/group). Arrows indicate microglia in A and D. **(F, G, and J)** Representative images of IF of Qki and EYFP (F), quantification of percentage of Qki$^+$EYFP$^+$ microglia (G), and total number of EYFP$^+$ microglia (J) in the cortex of P21 *Qk*-iCKO mice and control mice injected with tamoxifen at P15 (n = 4 mice/group). **(H, I, and K)** Representative images of IF of Qki and EYFP (H), quantification of percentage of Qki$^+$EYFP$^+$ microglia (I), and total number of EYFP$^+$ microglia (K) in the CC of *Qk*-iCKO mice and control mice injected with tamoxifen at 8 wk of age and which subsequently received a CPZ diet for 4 wk (n = 4 mice/group). Scale bars: 50 µm. Data are means ± SD. Statistics were calculated using unpaired two-tailed Student's t test (B, E, and I–K). **, P < 0.01; ****, P < 0.0001. Ctrl, control; n.s., not significant.

effect of CPZ on microglia rather than an effect of the demyelination itself. To that end, we sought to determine the Qki protein level in mice treated with CPZ for only 2 wk, a time point that has not started to show demyelination yet (Fig. S1 A, middle panels), which was consistent with previous studies (Gudi et al., 2014; Praet et al., 2014). Immunofluorescence (IF) costaining of Qki and EYFP showed that there was no obvious difference in the level of Qki protein in microglia in the CC between mice treated with CPZ for 2 wk and control mice (Fig. S1 C). These data indicate that up-regulation of Qki in microglia was induced by myelin debris in the CPZ-induced demyelinating lesions rather than by the CPZ itself, which is consistent with previous

studies showing that CPZ specifically impacted mature oligodendrocytes but not other cell types (Gudi et al., 2014; Praet et al., 2014).

One of the major functions of microglia in demyelination is to remove myelin debris through phagocytosis; and various components of phagosomes have been shown to be up-regulated in response to demyelination (Olah et al., 2012). We then sought to compare elevated Qki with the level of phagocytic machinery components and known phagolysosome regulators in response to demyelination. Western blotting showed an over 10-fold increase in the phagolysosomal components Lamp1 and Lamp2 in freshly isolated microglia from the CC of mice treated for 4 wk with CPZ compared with those from controls (Fig. 1 C), indicating that phagocytic machinery in microglia was greatly up-regulated in response to CPZ-induced demyelination.

Moreover, lysosomal activity indicated by LysoTracker (Fig. S1 D), as well as the functional phagocytic activity indicated by uptake of pHrodo Red *Escherichia coli* BioParticle conjugates (Fig. S1 E), was also significantly increased in microglia isolated from the CC of mice treated with CPZ for 4 wk compared with microglia from control mice. Consistent with IF (Fig. 1, A and B), Western blot confirmed that Qki protein level was increased ∼10-fold in freshly isolated microglia from the CC of mice treated with the CPZ diet for 4 wk compared with that from controls (Fig. 1 C), indicating a great correlation of Qki protein level with phagocytic machinery assembling. The Mitf/Tfeb/Tfe3 family of transcription factors has been implicated in regulating phagocytosis, but we only observed 1.4-fold and 1.7-fold increases of Mitf and Tfe3, respectively, in microglia in response to CPZ-induced demyelination (the Tfeb level was too low to be detected in microglia; Fig. 1 C), indicating that although the Mitf/Tfeb/Tfe3 family of transcription factors might play a role in microglial phagocytosis, the expression of these transcriptional factors does not have a significant association with CPZ-induced demyelination. Taken together, these data suggest that Qki might be an important regulator of phagocytosis in microglia, which was induced in response to demyelination to a similar extent as were the major phagocytic machinery components Lamp1 and Lamp2.

To investigate the human disease relevance of the expression of Qki protein level in response to human demyelinating conditions, we investigated the expression of Qki protein in microglia/macrophages in a small cohort of human multiple sclerosis (MS) samples and control white matter from donors without neurological diseases (Table S1). Similar to the up-regulation of Qki in microglia in CPZ-treated mice, the level of QKI in microglia was also increased 3.2-fold in MS lesions compared with that in control white matter (Fig. 1, D and E). Taken together, our results demonstrate that Qki might play an important role in the phagocytosis of microglia in response to demyelinating conditions in both the mouse and human.

Deletion of Qk does not impair microgliosis in response to CPZ-induced demyelination

To investigate the role of Qki in the phagocytic activity of microglia in vivo, we generated a cohort of *Cx3cr1*$^{CreER\text{-}EYFP+/-}$; *Qk*$^{L/L}$ mice, in which tamoxifen-inducible Cre recombinase (CreER) is under the control of the endogenous promoter of *Cx3cr1*, a macrophage/microglia–specific gene. The *Cx3cr1*$^{CreER\text{-}EYFP+/-}$ allele in the *Cx3cr1*$^{CreER\text{-}EYFP+/-}$; *Qk*$^{L/L}$ cohort allows microglia-specific *Qk* knockout in brain with tamoxifen treatment (hereafter denoted as *Qk*-inducible conditional knockout [*Qk*-iCKO] mice). We found that there were no significant differences between *Cx3cr1* heterozygous *Cx3cr1*$^{CreER\text{-}EYFP+/-}$ mice and *Cx3cr1* wild-type mice (*Cx3cr1*^{wt}) regarding microglial phagocytosis and the response to CPZ-induced demyelination (Fig. S2, A–D). Therefore, age-matched *Cx3cr1*$^{CreER\text{-}EYFP+/-}$; *Qk*$^{L/+}$ or *Cx3cr1*$^{CreER\text{-}EYFP+/-}$; *Qk*$^{+/+}$ littermates with tamoxifen treatment were hereafter used as control mice in order to maintain the same genetic background regarding Cx3cr1 expression. IF costaining of EYFP and Qki showed that almost 100% of EYFP$^+$ microglia in control mice were Qki positive, but ∼4.5% of EYFP$^+$ cells in the *Qk*-iCKO mice were Qki positive (Fig. 1, F and G). In addition, the expression of Qki in Gfap$^+$ astrocyte and Olig2$^+$ oligodendrocyte lineage cells was not affected in *Qk*-iCKO mice (Fig. S3, A and B), further confirming that the depletion of Qki was specifically restricted in microglia in brain.

To determine the efficiency of depletion of Qki under demyelinating conditions, 8-wk-old *Qk*-iCKO and control mice were injected with tamoxifen and were then monitored while receiving 4 wk of CPZ treatment to induce myelin damage. We found that ∼93.9% of the EYFP$^+$ cells lacked the expression of Qki in the CC of *Qk*-iCKO mice, whereas almost 100% of the microglia in the CC of control mice were Qki positive (Fig. 1, H and I). These data indicate that Qki could be highly efficiently deleted in microglia under both physiological and demyelinating conditions. Importantly, under both conditions, we found that depletion of Qki did not affect microgliosis (Fig. 1, J and K), as indicated by similar numbers of EYFP$^+$ microglia in both *Qk*-iCKO mice and control mice.

Depletion of Qki in microglia does not affect CPZ-induced myelin damage but does impair myelin debris removal

To determine the impact of depletion of Qki in microglia on CPZ-induced demyelination in vivo, the *Qk*-iCKO mice and control mice were injected with tamoxifen at 2 wk of age and again at 8 wk of age, followed by dietary CPZ treatment for up to 6 wk to induce demyelination (Fig. 2 A). Consistent with previous reports (Gudi et al., 2014; Praet et al., 2014), CPZ-induced demyelination peaked at 4 wk, as indicated by unstructured myelin basic protein (Mbp) staining (Fig. 2, B and C). Transmission electron microscopy (TEM) was further used to determine the structure of myelin, which also indicated that the ratio of unstructured myelin to intact myelin reached the highest level at 4 wk after CPZ treatment (Fig. 2, D and E). Interestingly, there was no difference between *Qk*-iCKO mice and control mice regarding myelin structures, both before CPZ treatment and after 4 wk of it (Fig. 2, B–E), indicating that depletion of Qki in microglia affected neither the overall structure of myelin in the resting condition nor myelin damage in response to CPZ treatment. Reinforcing the notion that depletion of Qki in microglia did not affect oligodendrocyte killing or myelin damage induced by CPZ treatment, there was no difference in the number of oligodendrocyte numbers in the CC of *Qk*-iCKO mice and control mice either before CPZ treatment or after 4 wk of it (Fig. S3 C).

Previous studies have shown that CPZ-induced myelin debris can be mostly cleared up by microglia within 2 wk after their numbers peak (Gao and Tsirka, 2011). Consistent with previous studies, in control mice we observed almost complete clearance of unstructured myelin at 6 wk after CPZ treatment started. However, in the *Qk*-iCKO mice, 37.8% of myelin still remained, which was indicated by IF staining of Mbp (Fig. 2, B and C). Consistent with IF staining, TEM analysis also confirmed that 36% of the axons in the CC of *Qk*-iCKO mice still contained myelin sheaths; among these axons, 91.4% were unstructured myelin sheaths that were characterized by at least one feature of splits, sheath breakdown, or vacuolated formations (Fig. 2, D and E). These results indicate that depletion of Qki in microglia did not affect CPZ-induced myelin damage but greatly delayed myelin debris clearance by microglia.

After being taken up by microglia/macrophages, lipid-rich myelin debris often accumulates as lipid drops in the cytoplasm of these cells, resulting in lipid-laden microglia/macrophages (LLM; Cantuti-Castelvetri et al., 2018; Raine et al., 1981). To evaluate whether depletion of Qki affects lipid droplet accumulation in microglia during CPZ-induced demyelination, lipid droplets in the microglia were evaluated by TEM from the CC of *Qk*-iCKO mice and control mice. We found that LLM from the CC of regular diet–fed *Qk*-iCKO and control mice were undetectable, indicating that Qki loss does not significantly affect the formation of lipid droplets in microglia in the resting condition (Fig. 2 F, left panels; and Fig. 2 G). However, after 4 wk of CPZ-diet treatment to induce massive myelin debris, control mice displayed more LLM than did *Qk*-iCKO mice, indicating that depletion of Qki reduces the ability of microglia to take up myelin debris (Fig. 2 F, middle panels; and Fig. 2 G). However, after 6 wk of CPZ-diet treatment, significantly more LLM were found in *Qk*-iCKO mice than in control mice (Fig. 2 F, right panels; and Fig. 2 G), indicating that compared with the uptake of myelin debris, the degradation of myelin debris was more significantly impaired by Qki loss in microglia. Taken together, these results indicate that Qki loss in microglia significantly diminished both the uptake and the degradation of myelin debris, leading to first reduction and then accumulation of LLM in *Qk*-iCKO mice during the CPZ-induced demyelinating process.

Microgliosis and axonal damage are two characteristics of CPZ-induced demyelination. The extent of microgliosis and damaged axons has been shown to correlate with that of damaged myelin debris during the demyelinating process (Gao and Tsirka, 2011). Consistent with large areas of unstructured myelin being present in *Qk*-iCKO mice with 6 wk of treatment (Fig. 2, B and D), there was a significantly higher level of microgliosis, which was indicated by Iba1 staining (Fig. 2, H and I), and axonal damage, which was indicated by amyloid precursor protein (APP; Fig. 2, J and K) and synaptophysin (Fig. S3 D) staining, in the CC of *Qk*-iCKO mice than in that of control mice. Since *Qk*-iCKO mice and control mice had no differences in microgliosis (Fig. 2, H and I) and axon damage (Fig. 2, J and K; and Fig. S3 D), either before CPZ treatment or after 4 wk of it, the persistent microgliosis and axonal damage in *Qk*-iCKO mice with 6 wk of treatment were more likely associated with unsolved myelin debris than by depletion of Qki in the microglia directly. Taken together, these data show that depletion of Qki significantly impaired the ability of microglia to clear up the damaged myelin debris and subsequently led to persistent microgliosis and axonal damage, suggesting that Qki may regulate the phagocytic activity of microglia during demyelinating processes.

Depletion of Qki impaired the phagocytic function of microglia in CPZ-induced demyelination

To investigate the underlying mechanism of how depletion of Qki in microglia decreased microglial phagocytic activity and impaired myelin debris clearance during CPZ-induced demyelination, transcriptomic profiling was performed on microglia isolated from the CC of CPZ-treated *Qk*-iCKO mice and control mice. Analysis of the differentially expressed genes identified 1,035 genes that were significantly up-regulated and 1,327 genes that were significantly down-regulated ($q < 0.05$; fold change >1.2-fold) in Qki-depleted microglia compared with control microglia (Fig. S4 A). Pathway analysis enriched 31 pathways that were significantly changed by depletion of Qki ($P < 0.05$; Fig. 3 A). Among them, phagosome formation is the top down-regulated pathway. Other pathways that are related to phagosome formation and/or activity, such as antigen processing presentation, tight junctions, peroxisome proliferator–activated receptor (PPAR) signaling pathway, and extracellular matrix–receptor interaction, were also significantly down-regulated (Fig. 3 A), indicating that Qki modulates the phagocytic function of microglia in response to CPZ-induced demyelination through regulating the genes involved in phagosome formation and activity. The down-regulated genes involved in phagocytosis include genes encoding receptors in phagosome initiation (e.g., *Cd36* and *C1Ra*), phagosome signal transduction proteins (e.g., *Rac1*), phagosome maturation factor (e.g., *Cnn1*), and lipid metabolic enzymes involved in phagosome membrane modulation (e.g., *Scd1* and *Scd2*; Fig. 3 B); among these genes, we were able to verify the top 10 through quantitative PCR (qPCR; Fig. 3 C).

Besides regulating mRNA homeostasis and stability, Qki, as an RNA-binding protein, has been reported to regulate alternative splicing (Darbelli and Richard, 2016). By analyzing the transcriptomic dataset with the Multivariate Analysis of Transcript Splicing (4.0.2) platform, we identified 632 genes that were changed at the splicing level ($P < 0.05$; fold change >1.2-fold) by Qki depletion in microglia (Table S2). Pathway analysis on these genes also identified the phagosome pathway as one of the most enriched pathways (Fig. S4 B). Taken together, these results demonstrated that Qki can regulate the genes that are involved in phagocytosis by modulating both their RNA stability and splicing, which is consistent with our previous study (Shingu et al., 2017).

To evaluate the impacts of Qki deficiency on microglial phagocytic activity, we isolated microglia from *Qk*-iCKO mice and control mice and applied the phagocytic assays in vitro. We found that depletion of Qki in microglia reduced their ability to engulf pHrodo Red *E. coli* BioParticle conjugates by 80% (Fig. 3 D). To specifically determine the impact of Qki on the uptake of myelin debris in vitro, isolated myelin debris was incubated with the isolated microglia, and its uptake was determined by IF staining of myelin protein Mbp within the

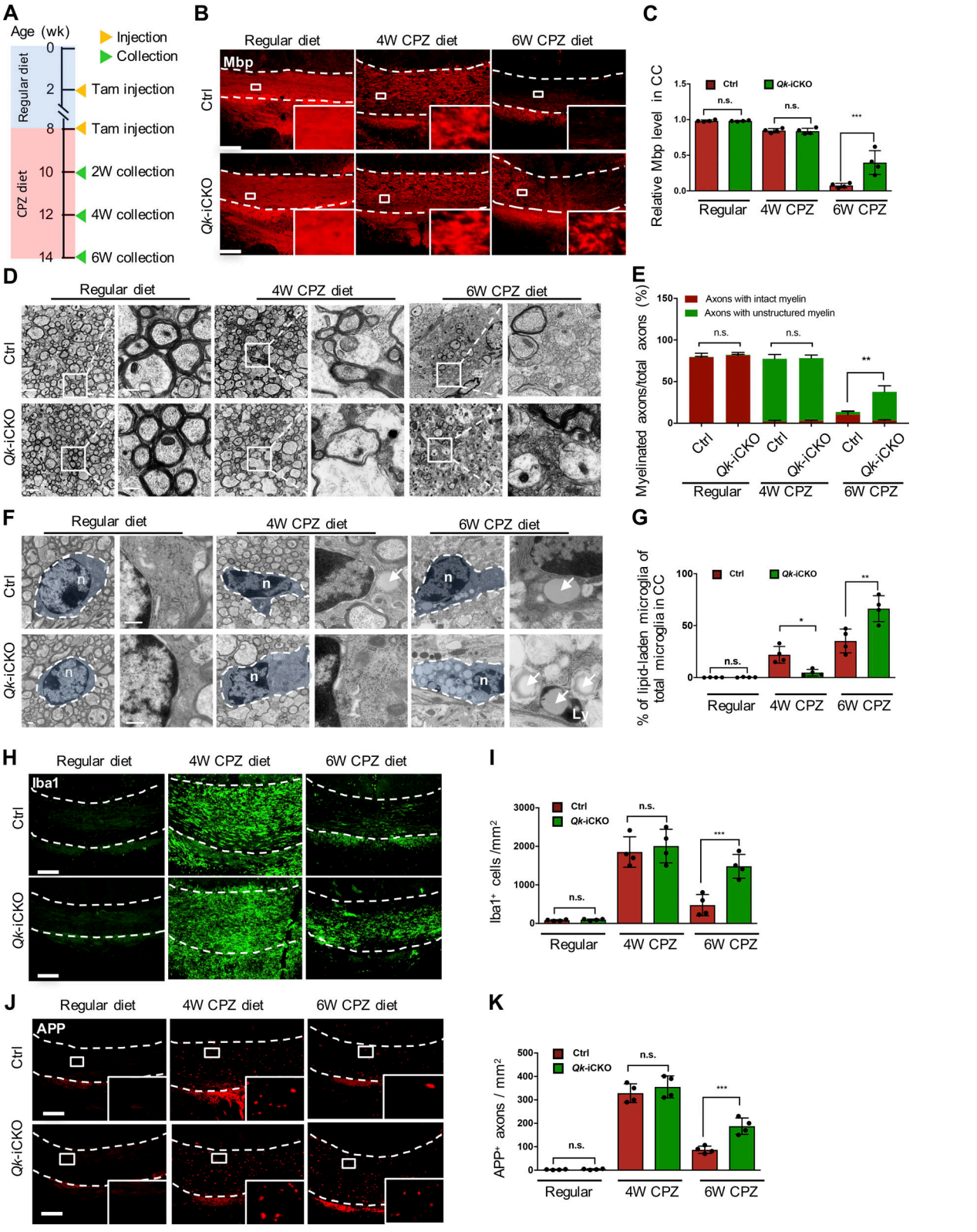

Figure 2. **Depletion of Qki in microglia does not affect CPZ-induced myelin degeneration but impairs myelin debris removal. (A)** Schema representing the experimental design for tamoxifen (Tam) injection, CPZ diet treatment, and sample collection. **(B and C)** Representative images of IF and quantification of Mbp in the CCs of 8-wk-old *Qk*-iCKO and control mice with tamoxifen injection followed by 4- or 6-wk administration of the CPZ diet (n = 4 mice/group). **(D)** Representative electron micrographs of myelin in the CCs of 8-wk-old *Qk*-iCKO and control mice with tamoxifen injection followed by 4- or 6-wk administration of the CPZ diet (n = 4 mice/group). **(E)** Quantification of the percentages of axons wrapped with intact myelin or unstructured myelin of the samples in D. **(F)** Representative electron micrographs showing the morphology and LLM in the samples in D (n = 4 mice/group). Arrows indicate lipid droplets. Ly, lysosome; n, nucleus. **(G)** Quantification of the percentages of LLM of the samples in F. **(H and I)** Representative images of IF and quantification of Iba1 in

the CCs of 8-wk-old *Qk*-iCKO and control mice with tamoxifen injection followed by 4- or 6-wk administration of the CPZ diet (n = 4 mice/group). **(J and K)** Representative images of IF and quantification of APP in the CCs of 8-wk-old *Qk*-iCKO and control mice with tamoxifen injection followed by 4- or 6-wk administration of the CPZ diet (n = 4 mice/group). Scale bars: 100 µm in B, H, and J; 2 µm in D; and 500 nm in F. Data are means ± SD. Statistics were calculated using two-way ANOVA with Tukey's post hoc tests (C, G, I, and K) and χ^2 test (E). *, P < 0.05; **, P < 0.01; ***, P < 0.001. n.s., not significant. The regions between the dashed lines (B, H, and J) indicate the CC. Data are representative of three independent experiments (B, C, J, and K). Ctrl, control; W, week.

microglia. With this assay, we found that depletion of Qki reduced the ability of microglia to engulf myelin debris by 74% (Fig. 3 E). These data demonstrate that loss of Qki significantly impaired microglial phagocytosis.

To further reinforce that depletion of Qki attenuated the phagocytic activity of microglia during CPZ-induced demyelination in vivo, the colocalization rate of myelin debris (indicated by Mbp staining) and microglia colocalization (indicated by EYFP staining) were determined in *Qk*-iCKO mice that received a 4-wk CPZ diet and control mice, groups that had a similar level of Mbp intensity (Fig. 2, B and C) and comparable microglial cell numbers (Fig. 2, H and I). As shown in Fig. 3, F–H, microglia from *Qk*-iCKO mice exhibited significantly fewer colocalizations of Mbp and EYFP than control microglia in the demyelinating lesion, indicating that *Qk*-iCKO mice had impaired myelin debris uptake compared with control mice. Taken together, our study demonstrated that depletion of Qki in microglia greatly impaired the phagocytic activity of microglia but not microgliosis, suggesting that Qki is an important regulator of the phagocytic activity of microglia.

Qki regulates various genes involved in phagocytosis through interacting with their RNA

As an RNA-binding protein, Qki has been reported to regulate mRNA homeostasis, stability, and splicing through interacting directly with the Qki-binding motif (A)CUAAY (where Y is C or U) of these mRNA (Galarneau and Richard, 2005). Therefore, we tested the interaction of Qki with the top 10 phagocytosis genes whose expression levels were down-regulated by depletion of Qki (Fig. 3 C) through the RNA immunoprecipitation (RIP) assay coupled with qPCR. We found that Qki could interact with 9 of 10 targets in mouse microglia EOC 20 cells (Fig. 4 A) and all 10 targets in mouse macrophage RAW 264.7 cells (Fig. 4 B). Among these targets, Cd36 has been shown to be important for microglia/macrophage phagocytosis under neurodegenerative conditions (Fu et al., 2014; Yamanaka et al., 2012). To determine whether Cd36 also plays a role in microglial phagocytosis under demyelinating conditions, we inhibited its activity with sulfo-N-succinimidyl oleate (SSO; Kuda et al., 2013) and found that inhibition of Cd36 significantly decreased the uptake of pHrodo Red *E. coli* BioParticle conjugates (Fig. 4 C) as well as CFSE-labeled mouse myelin debris (Fig. 4 D) in both EOC 20 and RAW 264.7 cells.

Next, we sought to assess the epistatic interaction between Qki and Cd36 in the regulation of phagocytosis using the mouse Raw 264.7 cell line. Consistent with the transcriptomic data (Fig. 3, B and C), knockdown of Qki with three independent siRNAs significantly reduced the protein level of Cd36 (Fig. S5 A). More importantly, ectopic expression of Cd36 (Fig. S5 B) significantly (albeit partially) restored the uptake of pHrodo Red *E. coli* BioParticle conjugates (Fig. 4 E) and CSFE-labeled mouse myelin debris (Fig. 4 F) in Qki knockdown Raw 264.7 cells. Together, these data indicate that Qki regulates microglial phagocytosis of myelin debris by directly modulating the RNA stability of genes involved in phagocytosis and that Cd36 is one of the targets of Qki to mediate its regulation of phagocytosis.

Persistent myelin debris impaired proper remyelination in Qki-depleted mice

Numerous studies have shown that persistent myelin debris can affect the remyelinating process (Lampron et al., 2015; Natrajan et al., 2015). To investigate the impact of persistent myelin debris resulting from Qki deficiency–defective phagocytic activity on remyelination, *Qk*-iCKO mice and control mice that had been treated with dietary CPZ for 6 wk were switched to a regular diet for 3 wk to allow remyelination to take place (Fig. 5, A and B). Consistent with previous studies (Praet et al., 2014), we found that 76.2% of the CCs in control mice fed the regular diet for 3 wk had been remyelinated, as shown by IF staining of Mbp. In contrast, only 44.6% of the CCs were covered with myelin in *Qk*-iCKO mice (Fig. 5, C and D), indicating that *Qk*-iCKO mice were less efficient than control mice in the process of remyelination. Since Mbp staining does not necessarily indicate compact myelin formation, nor does it reveal the detailed axon structure, TEM was used to quantify myelinated axons in the CC. Consistent with the IF staining of Mbp, TEM showed that 53.5% of the axons in the CCs of control mice had been myelinated, whereas only 34.6% of the axons were myelinated in *Qk*-iCKO mice (Fig. 5, E and F). Furthermore, analysis of myelin integrity with TEM demonstrated that only 4.7% of the myelin in the CCs of control mice was unstructured myelin, whereas the frequency of unstructured myelin was 28.9% in the CCs of *Qk*-iCKO mice (Fig. 5, E and F). Lastly, the g-ratio (the ratio of the inner axonal diameter to the total outer diameter) in the CCs of *Qk*-iCKO mice was significantly increased compared with that of control mice, revealing a marked reduction in myelin thickness (Fig. 5 G), whereas the axonal density (Fig. 5 H) and axonal diameters (Fig. 5 I) were not affected by depletion of Qki in the microglia. In addition, there were significantly more LLM in *Qk*-iCKO mice than in control mice after release from the CPZ diet for 3 wk (Fig. 5, J and K), reinforcing the impaired phagocytosis of myelin debris induced by Qki depletion in microglia. Collectively, these results indicate that damaged myelin was still persistent during the recovery period and that remyelination was significantly impaired in *Qk*-iCKO mice, suggesting that Qki-regulated microglial phagocytosis is crucial for myelin debris clearance and subsequent proper remyelination.

Previous studies of toxin-induced demyelination in animal models demonstrated that remyelination was mediated by OPCs, which responded to chemotactic cues, migrated into the

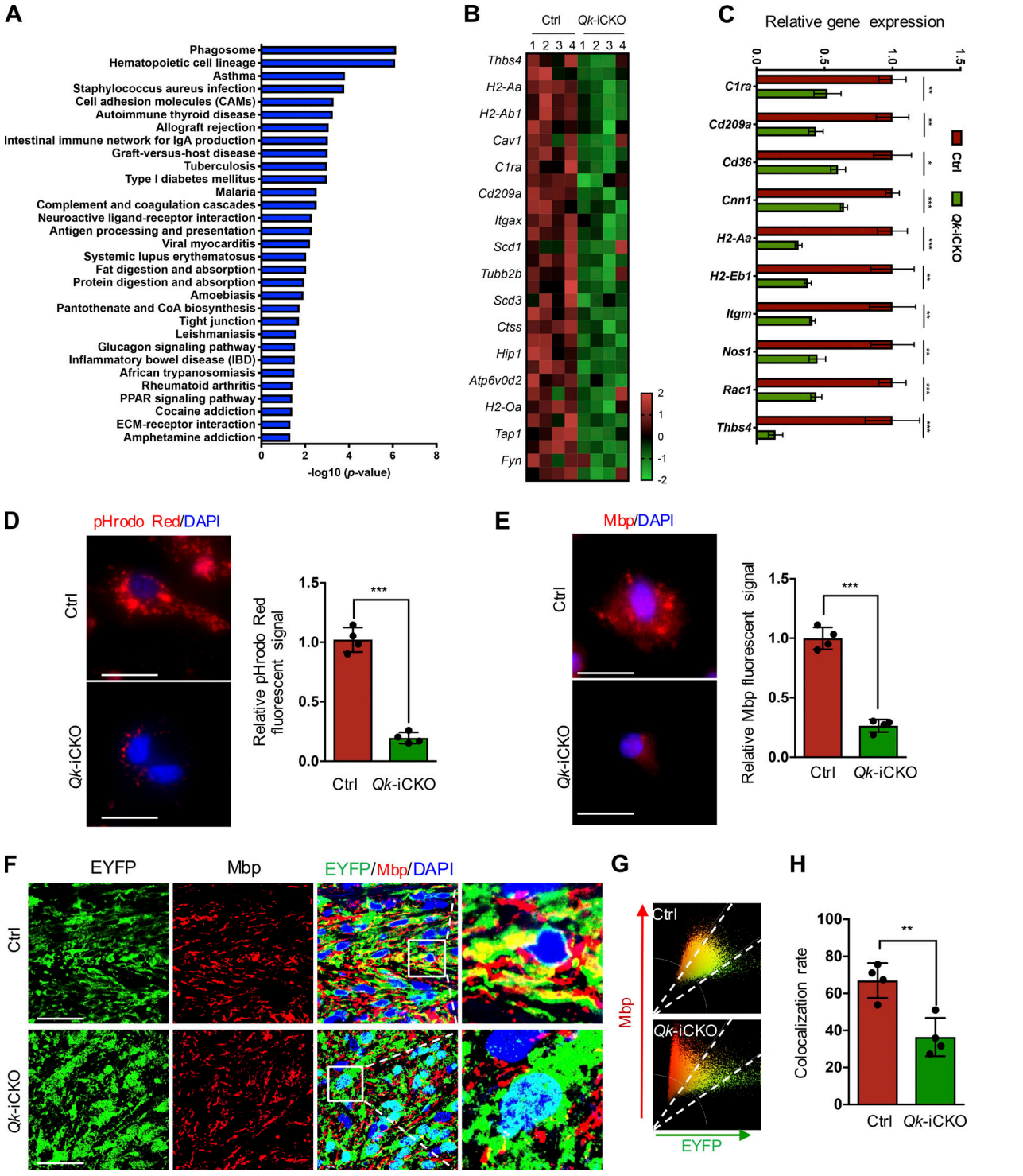

Figure 3. **Depletion of Qki in microglia impaired its transcription of genes involved in phagocytic activity. (A)** Bar graph showing the enriched pathways based on the differentially expressed genes in microglia isolated from 8-wk-old *Qk*-iCKO mice and control mice with tamoxifen injection followed by 6-wk administration of the CPZ diet (n = 4 samples/group). **(B)** Heatmap representing down-regulated genes involved in phagocytosis in microglia of the samples in A. **(C)** qPCR validation of the top 10 down-regulated genes involved in phagocytosis in microglia of the samples in A. **(D)** Representative images and quantification of the uptake of pHrodo Red *E. coli* BioParticles conjugates in isolated microglia from P21 *Qk*-iCKO and control mice injected with tamoxifen at P15 (n = 4 mice/group; at least 50 cells/mouse were counted and quantified). **(E)** Representative images and quantification of Mbp, an indicator for uptaken myelin debris in isolated microglia from P21 *Qk*-iCKO and control mice injected with tamoxifen at P15 (n = 4 mice/group; at least 50 cells/mouse were counted and quantified). **(F)** Representative images of IF of Mbp and EYFP in the CCs of 8-wk-old *Qk*-iCKO mice and control mice with tamoxifen injection followed by 4-wk administration of the CPZ diet (n = 4 mice/group). **(G)** Scatter plot showing the colocalization rates of Mbp and EYFP for the images in F; the signals with colocalization of Mbp and EYFP are indicated between the dashed lines. **(H)** Quantitative analyses of colocalization rate from the samples in F. Scale bars: 25 µm in D and E; 50 µm in F. Data are means ± SD. Statistics were calculated using unpaired two-tailed Student's t test (C–E and H). *, P < 0.05; **, P < 0.01; ***, P < 0.001. Data are representative of three independent experiments (C, D, and E). Ctrl, control; CoA, coenzyme A; ECM, extracellular matrix; PPAR, peroxisome proliferator–activated receptor.

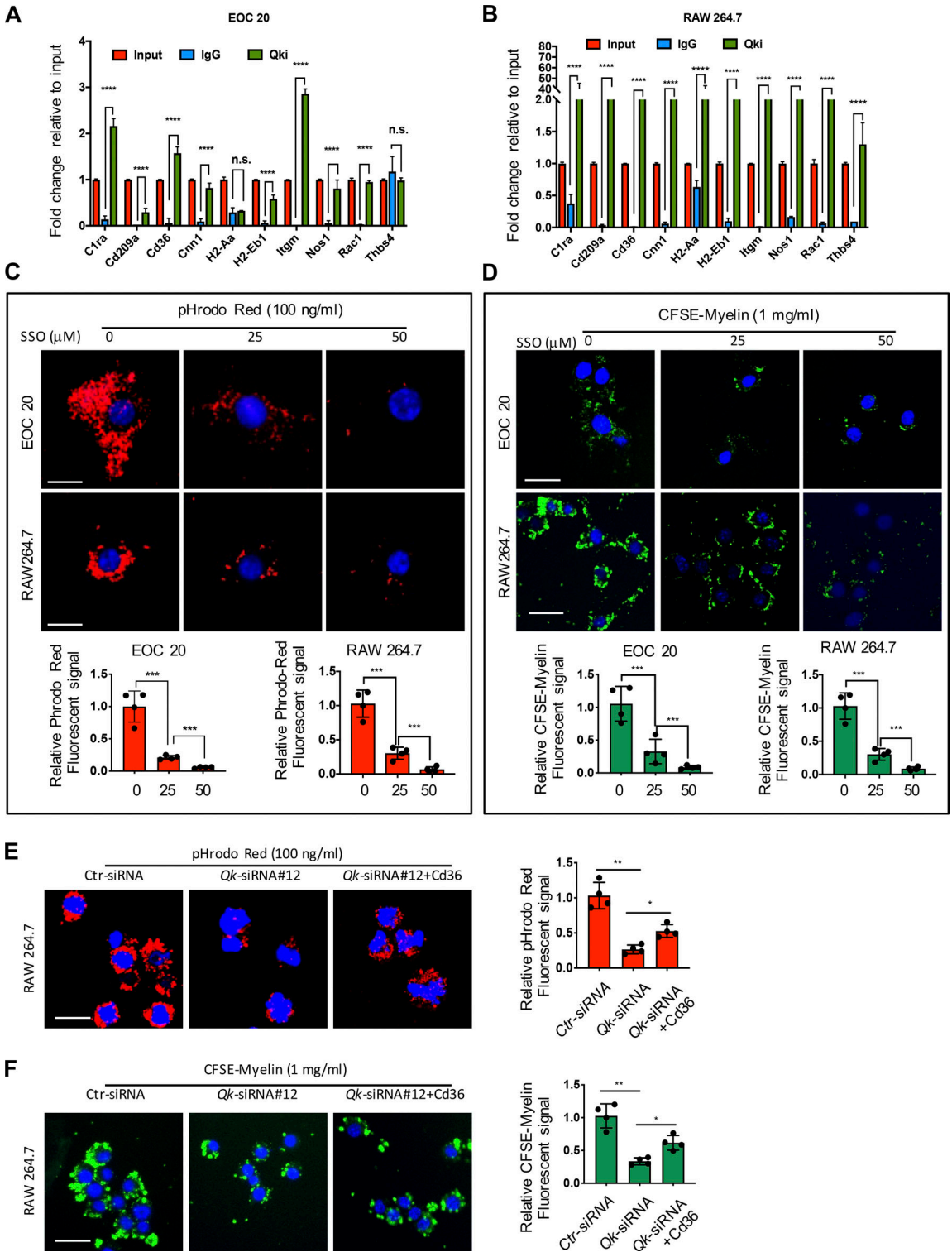

Figure 4. **Qki regulates various genes involved in phagocytosis in microglia through interacting with their RNAs. (A and B)** Qki target RNAs were immunoprecipitated with normal rabbit IgG or antibody against Qki following the RIP method in EOC 20 and RAW 264.7 cell lines, respectively. The abundance of immunoprecipitated RNAs was measured by qPCR and normalized against the levels of input. **(C)** Representative images and quantification of the uptake of pHrodo Red *E. coli* BioParticle Conjugates by EOC 20 and RAW 264.7 cells treated with Cd36 inhibitors (n = 4/group; at least 50 cells/slide were counted and quantified). **(D)** Representative images and quantification of the uptake of CFSE-labeled myelin debris by EOC 20 and RAW 264.7 cells treated with Cd36 inhibitors (n = 4/group; at least 50 cells/slide were counted and quantified). **(E)** Representative images and quantification of the uptake of pHrodo Red *E. coli* BioParticle conjugates by RAW 264.7 cells with knockdown of Qki and ectopic expression of Cd36 (n = 4/group; at least 50 cells/slide were counted and quantified). **(F)** Representative images and quantification of the uptake of CFSE-labeled myelin debris by RAW 264.7 cells with knockdown of Qki and ectopic expression of Cd36 (n = 4/group; at least 50 cells/slide were counted and quantified). Scale bars: 10 μm in C and 20 μm in D–F. Data are means ± SD. Statistics were calculated using unpaired two-tailed Student's t test (A and B) and one-way ANOVA with Tukey's post hoc tests (C–F). *, P < 0.05; **, P < 0.01; ***, P < 0.001; ****, P < 0.0001; Data are representative of three independent experiments (A–F). Ctr, control; n.s., not significant.

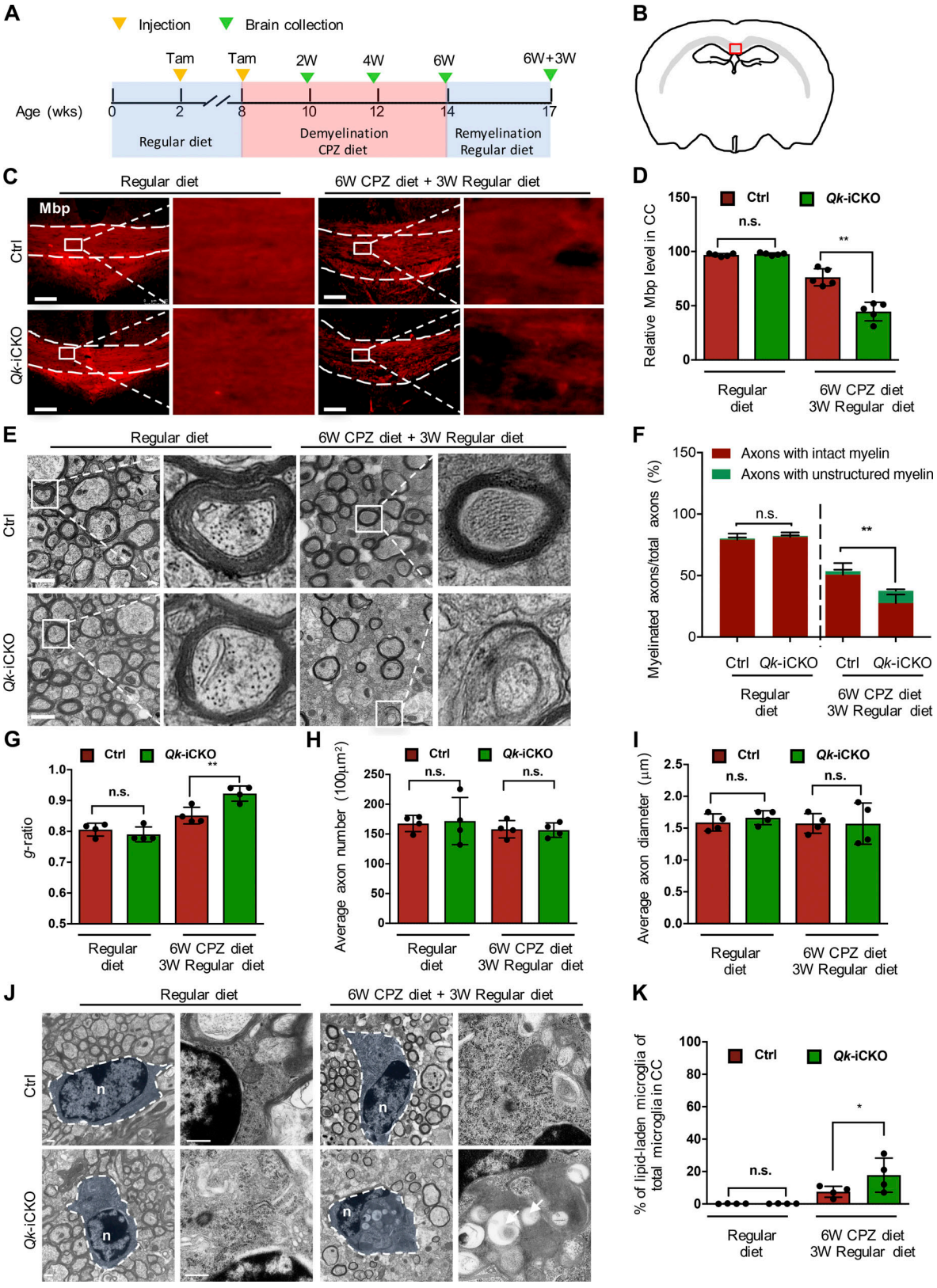

Figure 5. **Persistent myelin debris impaired proper remyelination in Qki-depleted mice. (A)** Schema representing the strategy of animal treatment and sample collection. Tam, tamoxifen. **(B)** Schema representing the examined coronal section of mouse brain. The red boxed area of the caudal CC was analyzed (modified from Sidman, High Resolution Mouse Brain Atlas; Sidman et al., 1999) in C, F, and J. **(C and D)** Representative images of IF and quantification of Mbp in the CCs of 8-wk-old *Qk*-iCKO mice and control mice with tamoxifen injection followed by 6-wk administration of the CPZ diet and 3 wk of the regular diet (n = 5 mice/group). **(E)** Representative electron micrographs of myelin in the CCs of 8-wk-old *Qk*-iCKO mice and control mice with tamoxifen injection followed

by 6-wk administration of the CPZ diet and 3 wk of the regular diet (n = 4 mice/group). **(F–I)** Quantification of the percentages of axons wrapped with intact myelin and unstructured myelin among the total axons (F), the g-ratio (G), the axon density (H), and the axonal diameter (I) in the CCs of the samples in E (n = 4 mice/group). **(J)** Representative electron micrographs showing the morphology and LLM in the samples in E (n = 4 mice/group. Arrows indicate lipid droplets. n, nucleus. **(K)** Quantification of the percentages of LLM of the samples in J (n = 4 mice/group). Scale bars: 100 µm in C, 2 µm in E, and 500 nm in J. Data are means ± SD. Statistics were calculated using two-way ANOVA with Tukey's post hoc tests (D, GI, and K) and χ^2 test (F). *, P < 0.05; **, P < 0.01. Ctrl, control; n.s., not significant; W, week.

demyelinating lesions, and differentiated into mature oligodendrocytes (Miron et al., 2011). To determine whether impaired remyelination induced by persistent myelin debris was due to either diminished recruitment of OPCs or compromised differentiation of OPCs into myelinating oligodendrocytes, *Qk*-iCKO mice and control mice that had been treated with dietary CPZ for 6 wk were switched to a regular diet for up to 3 wk to allow remyelination to take place (Fig. 6, A and B). Consistent with previous studies (Praet et al., 2014), we observed that platelet-derived growth factor receptor α (PDGFRα)$^+$ OPCs were recruited as early as 4 wk after CPZ treatment, and the numbers of OPCs reached a peak at 6 wk after CPZ-treatment and gradually declined during the release phase (remyelinating phase) with a regular diet; in addition, the numbers of PDGFRα$^+$ OPCs were comparable at all time points between the *Qk*-iCKO mice and control mice (Fig. 6, C and D). These results indicate that although deletion of *Qk* in microglia significantly slowed the clearance of myelin debris, it did not affect OPC recruitment and proliferation.

Then, we asked whether the differentiation of OPCs into myelinating oligodendrocytes was affected in *Qk*-iCKO mice during remyelination. With the same cohort, we found that the numbers of GSTπ$^+$ mature myelinating oligodendrocytes in *Qk*-iCKO mice were significantly less than those in control mice at all time points of the remyelinating phase (Fig. 6, E and F). Thus, these data indicate that impaired phagocytosis in Qki-depleted microglia slows down the clearance of myelin debris and further inhibits the differentiation of OPCs into myelinating oligodendrocytes, consequently delaying subsequent remyelination.

Discussion

As a dynamic biological process, phagocytosis plays a vital role throughout the life cycles of multicellular organisms (Underhill and Goodridge, 2012). Although some cellular insights regarding phagocytosis have been generated in recent years, owing to new tools in cell biology and microscopy, the detailed molecular mechanisms underpinning the way this highly coordinated phagocytic process is regulated are poorly understood, particularly with respect to various stress conditions (Uribe-Querol and Rosales, 2017; Wake et al., 2011). In this study, we identified Qki as a master regulator of phagocytosis in microglia in response to CPZ-induced demyelination by using a novel mouse model with microglia-specific *Qk* deletion. We found that depletion of Qki severely impaired the phagocytic activity of microglia by regulating the expression of various genes, such as those encoding the microglial phagocytic receptor: genes *Cd36*, *Cd209a*, and *C1Ra*; the signaling protein for activation of phagocytosis *Rac1*; and components involved in phagosome formation and maturation such as *Cav1*, *Cav2*, *Thbs4*, *Atp6v0d2*, *Itgb3*, *Itgam*, *Itgax*, and *Itgam*. Consistently, we found that depletion of Qki not only severely diminished the uptake of myelin debris in vitro (Fig. 3, D and E) and in vivo (Fig. 3, F–H) but also severely impaired the degradation of myelin debris in microglia, which led to accumulation of LLM (Fig. 2, F and G; and Fig. 5, J and K). Furthermore, compared with slightly increased expression of the Mitf/Tfeb/Tfe3 family of transcription factors in microglia, the expression of Qki protein in microglia was greatly increased and positively correlated with the increased assembly of phagocytic machinery in response to demyelination, suggesting that Qki might be a more important regulator than the Mitf/Tfeb/Tfe3 family of proteins in regulating phagocytosis in demyelination. Of translational significance, Qki was also found to be up-regulated in human microglia associated with MS demyelination. Taken together, our results indicate that Qki might be a general regulator of phagocytosis and endocytosis in various cell types and is implicated in playing a crucial role in demyelination that was not appreciated previously. Left unanswered is what leads to the up-regulation of Qki in microglia in response to demyelination, and further mechanistic studies are warranted to address this essential question.

Microglia are the major innate immune cells in the CNS, which originate from a myeloid lineage and populate the brain during early development (Lenz and Nelson, 2018). They not only maintain homoeostatic activity in the normal CNS but also rapidly respond to pathological conditions such as infection, stroke, or neurodegenerative processes. Under stress or during neurological diseases, microglia become activated, migrate to and within the lesions, release a wide range of soluble factors (including cytokines, neurotrophins, and immunomodulatory factors), and clear up cellular debris by phagocytosis (Li and Barres, 2018; Parkhurst et al., 2013). However, the question of whether microglia play harmful or beneficial roles in CNS injury and various diseases has been widely debated (Neumann et al., 2009). In this study, we found that impaired phagocytic activity of microglia by depletion of Qki impaired the clearance of myelin debris in the CC, which in turn resulted in accumulation of axonal damage, inhibition of the maturation of oligodendrocytes, and eventual delay of proper remyelination. It will be intriguing in the future to ascertain if Qki expression levels are associated with the persistence of MS plaques and tumefactive lesions.

Our findings are consistent with previous reports showing that microglia play a beneficial role for patients with demyelinating diseases (Lampron et al., 2015; Natrajan et al., 2015). For instance, Natrajan et al. (2015) reported that a decrease in phagocytic activity due to defective retinoid X receptor activity or Trem2 function in microglia impaired remyelination and

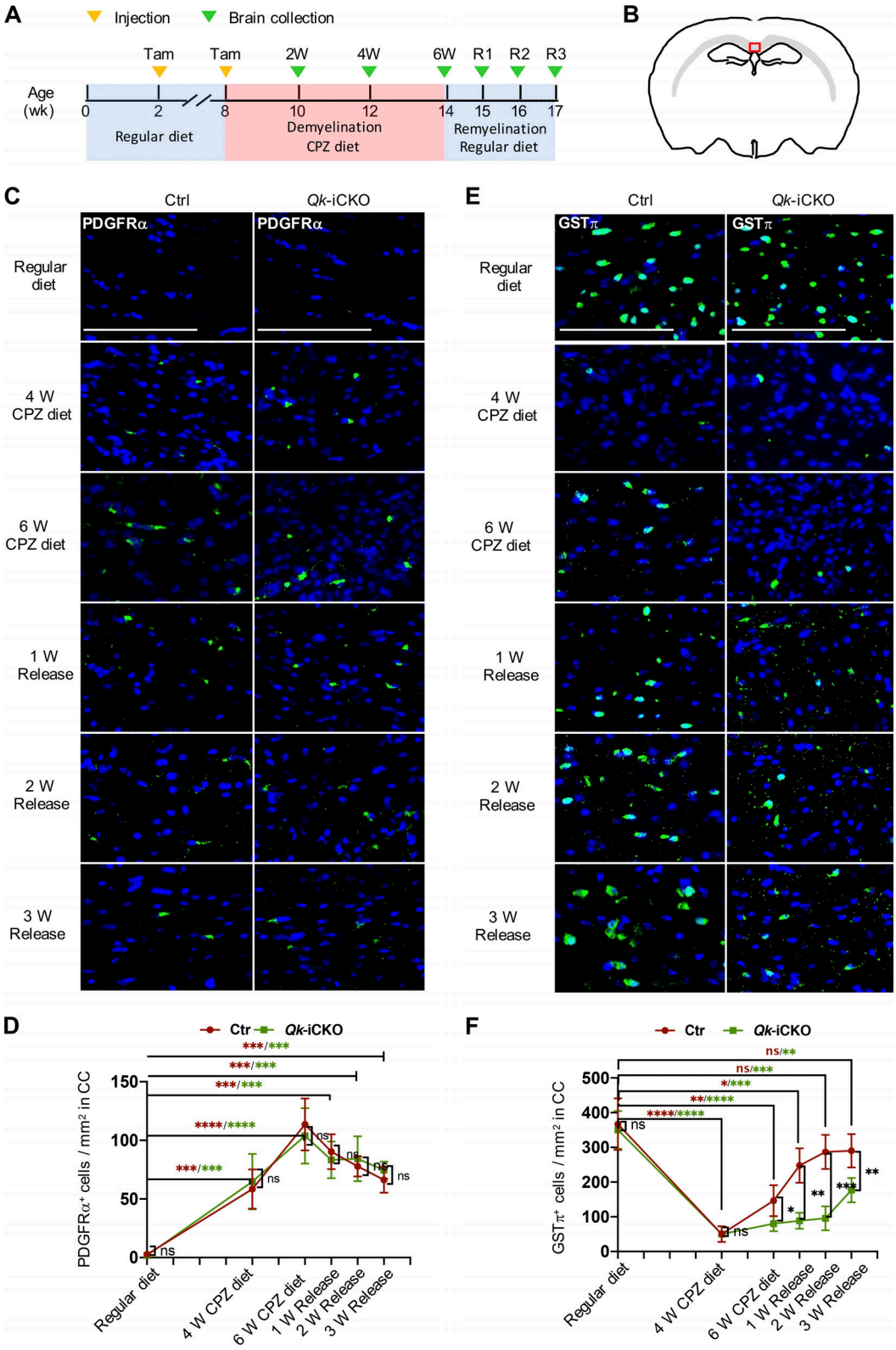

Figure 6. **Persistent myelin debris in the Qki-depleted mice delays differentiation of OPCs to myelinating oligodendrocytes. (A)** Schema representing the strategy of animal treatment and sample collection. Tam, tamoxifen. **(B)** Schema representing examined coronal section of the mouse brain. The red boxed area of the caudal CC was analyzed (modified from Sidman, High Resolution Mouse Brain Atlas; Sidman et al., 1999) in C–F. **(C and D)** Representative images of IF and quantification of PDGFRα in the CCs of 8-wk-old *Qk*-iCKO and control (Ctrl) mice with tamoxifen injection followed by either 4- or 6-wk administration of the CPZ diet or 6-wk administration of the CPZ diet and then 1, 2, or 3 wk of the regular diet. **(E and F)** Representative images of IF and quantification of GSTπ in the same regions described in C. *n* = 4/group. Scale bars: 100 µm. Data are means ± SD. Statistics were calculated using two-way ANOVA with Tukey's post hoc tests (D and F). *, P < 0.05; **, P < 0.01; ***, P < 0.001; ****, P < 0.0001. ns, not significant.

aggravated neurological dysfunctions. Recent findings in Alzheimer's disease also indicated that defects in microglial phagocytosis positively correlated with severity of disease development (Han et al., 2017; Janda et al., 2018; Krasemann et al., 2017). Overall, our studies and those of others have demonstrated that microglia play an instrumental role in myelin debris clearance through their phagocytic function, thereby playing a beneficial role in prevention of CNS diseases, particularly demyelinating diseases.

In contrast to the well-established role of microglia in CPZ-induced demyelinating conditions, the function of monocytes/macrophages under this condition has been controversial. Conflicting results have been reported regarding whether or not monocyte/macrophage infiltration actually happens in CPZ-induced demyelinating lesions (Ajami et al., 2007; Lampron et al., 2015; Mildner et al., 2007). In our model, the majority of EYFP-positive cells in demyelinating lesions were Qki negative after 4 wk of CPZ treatment (Fig. 1 H), indicating very minimal infiltration of macrophages in these lesions because macrophages would be Qki positive. Our data are consistent with previous findings that there is no profound infiltration of bone marrow–derived myeloid cells (Kondo et al., 1987; Mildner et al., 2007). A more consistent model system would have to be used to investigate the function of macrophages in demyelination.

Numerous studies have shown that the role of microglial phagocytosis in the pathogenesis of MS could be highly context dependent (Han et al., 2012; Lampron et al., 2015; Liu et al., 2015). For example, Han et al. (2012) showed that knockout of the "don't eat me" signal protein CD47 in mice greatly diminished the development of EAE, whereas blocking CD47 with a monoclonal antibody against it in mice at the peak of paralysis worsened EAE severity. CD47 was found mainly localizing on myelin, and down-regulation of CD47 enhanced phagocytosis of myelin, which supports our results that microglial phagocytosis is a main mechanism for myelin debris clearance. Due to the highly context-dependent yet extremely important function of microglial phagocytosis in the pathogenesis of MS, it would be worthwhile to investigate the function of Qki in microglial phagocytosis in different stages of demyelination as well as in different model systems, including EAE.

In conclusion, our findings reveal a key role for the RNA-binding protein Qki in regulating microglial phagocytosis during the course of demyelination and remyelination. Our results strongly suggest that the enhancement of phagocytosis by Qki may facilitate the neuroprotective function of microglia in response to CNS damage and neurological diseases, particularly demyelinating diseases. This study may lead to therapeutic opportunities by enhancing the phagocytic function of microglia in various CNS diseases, such as neurodegenerative diseases, demyelinating diseases, and brain tumors.

Materials and methods

Mice and CPZ treatment

C57BL/6 mice with the *Cx3cr1*$^{CreER\text{-}EYFP}$ alleles (stock no. 021160) were purchased from The Jackson Laboratory. The *Qk-loxP* allele was described previously (Shingu et al., 2017). C57BL/6 mice with *Qk-loxP* alleles were crossed with mice bearing *Cx3cr1*$^{CreER\text{-}EYFP}$ alleles to generate mice with the *Cx3cr1*$^{CreER\text{-}EYFP}$*; Qk*$^{L/+}$ or *Cx3cr1*$^{CreER\text{-}EYFP}$*; Qk*$^{+/+}$ and *Cx3cr1*$^{CreER\text{-}EYFP}$*; Qk*$^{L/L}$ genotype. Since the *Cx3cr1CreER-EYFP* allele is a knock-in allele, it will delete one allele of the *Cx3cr1* gene. To put experimental cohorts and control cohorts under the same genetic background, all mice used in this study had the heterozygous *Cx3cr1CreER-EYFP* alleles (*Cx3cr1CreER-EYFP*$^{+/-}$). Tamoxifen was dissolved in corn oil at the concentration of 10 mg/ml and was injected subcutaneously into mice of various ages on the basis of the following doses: for P14 mice, 20 µl tamoxifen was injected twice over 2 d consecutively; for 6–8-wk-old mice, 100 µl tamoxifen was injected twice over 2 d consecutively.

For demyelination, mice were injected with tamoxifen at P15 first and again at 8 wk of age. Then, the experimental mice were fed the 0.2% CPZ diet (TD140800; ENVIGO) for 2, 4, and 6 wk to induce demyelination. Control animals were fed a regular diet (TD140803; ENVIGO) and manipulated as often as 0.2% CPZ-fed mice. For remyelination, tamoxifen-injected 8-wk-old experimental mice were fed the 0.2% CPZ diet for 6 wk and then were switched to a regular diet for up to 3 wk to allow myelin recovery. The diet was changed every 2 d, and food intake was monitored throughout the protocols.

For IF and TEM analyses, four animals from each group were investigated at all time points, whereas four samples from each group (four brains were pooled together as one sample) were investigated for PCR, RNA sequencing, and alternative splicing analyses.

Brain dissection and sample preparation

Mice were overdosed with anesthetic or carbon dioxide, and their brains were removed with transcranial perfusion with 4% paraformaldehyde (PFA; EMS). The brains were fixed in formalin at room temperature for IF staining at 4°C in buffer containing 2% PFA and 3% glutaraldehyde for TEM. Formalin-fixed brain tissues were embedded in paraffin, and serial sections were prepared at 5-µm thickness and subjected to IF studies. For TEM, the fixed mouse brains were sent to the High-Resolution Electron Microscopy Facility at MD Anderson.

Microglia isolation

Microglia were isolated from the mouse brains (phagocytosis assay) or the dissected CC tissues of the experimental mice. In brief, mouse brains were removed or CC tissues were dissected, and single-cell suspensions were prepared using the Neural Tissue Dissociation Kit (Miltenyi Biotec) according to the manufacturer's instructions. Myelin debris was removed using Myelin Removal Beads II (Miltenyi Biotec), and microglia were then isolated using CD11b^{+} (microglia) Microbeads (Miltenyi Biotec) according to the manufacturer's instructions. The isolated microglia were further analyzed by flow cytometry with CD11b and CD45 antibodies to confirm that 93.5% of them were double positive for CD11b and CD45.

IF

For IF analysis of tissues, paraffin-embedded brain sections were treated by deparaffinization and antigen retrieval. After

blocking with the serum of goat or horse or bovine serum albumin, the samples were incubated with primary antibodies overnight at 4°C. Sections were stained with anti-Qki antibody (rabbit, 1:200; Bethyl Laboratories); anti-Iba1 antibody (goat, 1:500; Abcam); anti-GFP antibody (chicken, 1:200; Abcam); anti-Mbp antibody (mouse, 1:200; Covance); anti-Olig2 antibody (mouse, 1:200; EMD Millipore); anti-PDGFRα-2 antibody (rabbit, 1:200; Cell Signaling Technology); anti-GSTπ antibody (1:200; MBL International); anti-synaptophysin antibody (rabbit, 1:200; Abcam); and anti-APP antibody (1:500; Covance). The samples were then incubated with species-appropriate secondary antibodies from goat or donkey coupled with AlexaFluor dyes (488, 568, or 594; Thermo Fisher Scientific) for 1 h at room temperature at a dilution of 1:1,000. VECTASHIELD with DAPI (Vector Laboratories) was used to mount coverslips. IF images were taken with a Leica DMI8 inverted fluorescent microscope. For costaining, Z-stack images were taken. The colocolization analysis in Fig. 4 E was performed with the Leica LASX software package.

TEM

Mouse brains were transcardially perfused with 2% PFA and postfixed in a cold PBS buffer containing 3% glutaraldehyde and 2% PFA at 4°C. The dissected central part of the CC (1 mm in thickness) was washed in 0.1 M sodium cacodylate buffer and treated with 0.1% Millipore-filtered cacodylate-buffered tannic acid, postfixed with 1% buffered osmium tetroxide for 30 min, and stained en bloc with 1% Millipore-filtered uranyl acetate. The samples were dehydrated in increasing concentrations of ethanol and then infiltrated with and embedded in LX-112 medium. The samples were polymerized in a 600°C oven for approximately 3 d. Ultrathin sections were cut using a Leica Ultracut microtome, stained with uranyl acetate and lead citrate in a Leica EM Stainer, and examined in a JEM 1010 TEM (JEOL USA, Inc.) at an accelerating voltage of 80 kV. Digital images were obtained using an AMT Imaging System (Advanced Microscopy Techniques Corp). The total number of axons and myelinated axons was counted, and the percentage of myelinated axons was calculated using ImageJ software (National Institutes of Health) for further quantification (n = 4 fields/sample; n = 4 samples/group). According to the criteria established in the previous report (Skripuletz et al., 2013), myelin sheaths displaying splitting, breakdown, or vacuoles were determined to be unstructured myelin sheaths.

To evaluate LLM in the CC of brain during the demyelinating and remyelinating processes, the ultrathin sections from the CC of CPZ-treated mice and control mice were analyzed (four mice per group). Microglia were identified using a combination of ultrastructural characteristics, including a highly electron-dense cytoplasm and nucleus, an often star-shaped cell morphology, an irregularly shaped nucleus with coarsely clumped chromatin, and a cytoplasm rich in free ribosomes and vesicles (Cantuti-Castelvetri et al., 2018; Raine et al., 1981). Lipid droplets were identified as in previous publications (Fujimoto et al., 2013; Marschallinger et al., 2020). The cytoplasm and nucleus area were analyzed using ImageJ v.1.51s software. To analyze the percentage of lipid droplet–containing microglia, numbers of total microglia and of LLM were counted, and the percentage of LLM from total microglia was calculated and normalized.

RNA isolation and qPCR

The CC was dissected from brains of experimental mice using the dissecting microscope. Three dissected CCs were pooled as one sample for total RNA isolation. Total RNA was extracted from these tissues using the RNeasy Mini Kit (Qiagen) according to the manufacturer's protocols. The RNA concentration was measured with a NanoDrop 1000 device (Thermo Fisher Scientific). Complementary DNA was synthesized using the SuperScript III One-Step RT-PCR System with Platinum Taq DNA Polymerase (Thermo Fisher Scientific). Real-time qPCR analysis was performed using the iTaq Universal SYBR Green Supermix (Bio-Rad). All primers were exon spanning (Sigma-Aldrich). Gene expression of *C1ra*, *Cd209a*, *Cd36*, *Cnn1*, *H2-A2*, *H2-Eb1*, *Itgm*, *Nos1*, *Rac1*, and *Thbs4* was analyzed in the CC after 6 wk of CPZ treatment in *Qk*-iCKO mice and control mice. Information regarding the primers used is shown in Table S3. The ΔΔCt method was used to determine differences in gene expression between *Qk*-iCKO mice and control mice. Changes in mRNA expression levels were calculated after normalization to β-actin.

RNA sequencing and alternative splicing analyses

Microglia were isolated from the dissected CCs of *Qk*-iCKO mice and control mice treated with a CPZ diet for 6 wk. CCs from four mice of the same experimental group were pooled together as one sample and were used to isolate total RNA, and each experimental group had four samples. Total RNA sequencing was performed by the Illumina Next Generation Sequencing Service at the Sequencing and Microarray Facility of MD Anderson. RNA-sequencing data were analyzed using the typical RNA data analysis pipeline. In brief, the Tophat program was used to align raw reads with the mouse genome (mm10 version) with permission of two mismatches. After applying the easyRNA R package to extract the raw count tables based on the aligned bam files, we used edgR to perform normalization and differential gene expression analysis. The fold-change threshold at which genes were considered differentially expressed was set at 1.2-fold with $P < 0.05$. The differentially expressed genes were subjected to pathway enrichment using Advaita Bio's iPathwayGuide (http://www.advaitabio.com/ipathwayguide). Alternative splicing analyses were performed on the Multivariate Analysis of Transcript Splicing (4.0.2) platform. The detailed protocol is listed on the website (http://rnaseq-mats.sourceforge.net/rmats4.0.2/). The data have been deposited in the National Center for Biotechnology Information's Gene Expression Omnibus database (accession no. GSE121223).

Protein isolation and Western blot

Microglia were isolated from the dissected CC of mice fed the CPZ diet for 4 wk or from the whole brains of mice fed a regular diet. For the CPZ diet group, six dissected CCs were pooled together as one sample; for the regular diet group, four brains were pooled together as one sample. The fresh isolated microglia were harvested as described above, washed with PBS, lysed in RIPA buffer (150 mM NaCl, 50 mM Tris, pH 8.0, 1.0% Igepal

CA-630, 0.5% sodium deoxycholate, and 0.1% SDS; Sigma-Aldrich) with freshly added protease inhibitor cocktail tablet (cOmplete mini; Roche Diagnostics), phosphatase inhibitor cocktail 2 (Sigma-Aldrich), and 1 µM dithiothreitol and centrifuged at 10,000× *g* at 4°C for 15 min. The supernatant was used as the cell lysate in standard Western blot. Briefly, 20–50 µg of protein was subjected to 4%–12% gradient SDS-PAGE (NuPage; Thermo Fisher Scientific), transferred to a nitrocellulose membrane (Trans Blot Turbo; Bio-Rad), and incubated with the indicated primary antibodies (anti-Iba1: Wako, 1:500; anti-Qki, 1:1,000, Bethyl Laboratories; anti-Lamp1, 1:1,000, Abcam; anti-Lamp2, 1:1,000, Abcam; anti-Tfeb, 1:1,000, Cell Signaling Technology; anti-Mitf, 1:1,000, Abcam; and anti-Tfe3, 1:1,000, Sigma-Aldrich) followed by incubation with species-appropriate HRP-conjugated secondary antibodies. Bound antibodies were visualized using Super Signal, the enhanced chemiluminescence system (Thermo Fisher Scientific).

RIP assay and qPCR

RIP assay was performed in microglia cell line ECO 20 (ATCC CRL-2469) and macrophage cell line RAW 264.7 (ATCC TIB-71). Cell culture followed the guidelines of ATCC. EOC 20 cells were cultured using DMEM supplemented with 10% FBS and 100 U/ml of penicillin combined with 100 µg/ml of streptomycin (Gibco). RAW 264.7 cells were cultured using RPMI medium 1640 supplemented with 10% FBS and 100 U/ml of penicillin combined with 100 µg/ml of streptomycin. RIP was performed using the Magna Nuclear RIP kit according to the manufacturer's instructions (Sigma-Aldrich). Briefly, the cell lines were cultured to obtain a cell number of 5.0×10^6. The adherent cells were cross-linked using 0.3% PFA (EMS) in PBS for 10 min at room temperature, immediately after which excess PFA was quenched by adding glycine to a final concentration of 125 mM. Adherent cells were washed in PBS and collected from the dish through scraping. Extraction and lysis of the nuclei were completed with buffers provided within the Magna Nuclear RIP kit. The nuclear lysate was sonicated in ice-cold water for 15 pulses of 30 s each time, an optimized condition to attain sheared DNA fragments of 100–300 bps in size. Sheared chromatin was then treated with DNase I (Sigma-Aldrich) to degrade DNA. Immediately after DNase I treatment, nuclear lysate was mixed and incubated overnight at 4°C with protein A/G–conjugated magnetic beads (Sigma-Aldrich), which had been preincubated with 4 µg of rabbit anti-Qki antibody or normal rabbit IgG (2729S; Cell Signaling Technology). The beads were washed, and the protein–antibody complex was eluted by buffers provided within the Magna Nuclear RIP kit. RNA was extracted and purified from the eluate using TRIzol reagent (Thermo Fisher Scientific), further precipitated using linear polyacrylamide as a coprecipitant (GeneLink), and then resuspended in nuclease-free H_2O. Finally, DNase I treatment was repeated to degrade any remaining DNA contaminants before further analysis. The extracted RNA was reverse transcribed using SuperScript III Reverse Transcription (Thermo Fisher Scientific) and subjected to real-time qPCR using iTaq Universal SYBR Green Supermix. The sequences of all primers used in this study are shown in Table S3. The ΔΔCt method was used to determine differences in target mRNA between Qki antibody and normal IgG control. Changes in mRNA enrichment were calculated after normalization against the input.

siRNA-mediated Qki knockdown and Cd36 overexpression

The coding DNA sequence region of murine Cd36 from an ORF plasmid (MR227672; Origene) with an HA tag at the C-terminus was subcloned into the lentiviral vector pInducer20 (Meerbrey et al., 2011), and the lentiviruses packaged in HEK293T cells were used to infect RAW 264.7 cells. After selection with G418 (Thermo Fisher Scientific), the surviving cells were treated with doxycycline (Sigma-Aldrich) to induce the expression of Cd36-HA. RAW 264.7 cells with inducible Cd36-HA were seeded on coverslips in 12-well plates and transfected with 10 µM of *Qk*-targeting siRNAs (J042676-09; 5′-AAUUAGCAGAGUACGGAAA-3′; -10, 5′-GCACCUACAGAGACGCCAA-3′; -11, 5′-UGUACAAUG ACACGUUAAA-3′; and -12, 5′-GAUUGUGACCGCAGACCGA-3′; Dharmacon) and nontargeting pool (D0018101005; Dharmacon) using Lipofectamine RNAiMAX (13778150; Invitrogen) per manufacturer's instructions. 48 h after transfection, cells then were treated with 1 µg/ml of doxycycline for 24 h to induce Cd36-HA expression.

Myelin isolation and CFSE labeling

Myelin isolation and labeling with CFSE were performed as described by Rolfe et al. (2017). Briefly, 6–8-wk-old C57BL/6J mice were euthanized through CO_2 asphyxiation followed by cervical dislocation. Whole forebrains were dissected, placed onto a 100-mm dish on ice, and cut into small pieces with a scalpel until reaching a viscous semifluid consistency. The brain tissue was then transferred to a sterile glass Dounce homogenizer containing ice-cold 0.32 M sucrose–Tris-Cl solution and then grounded into a smooth homogenate. The brain homogenate in 0.32 M sucrose–Tris-Cl solution was then gently transferred onto the top of ice-cold 0.83 M sucrose–Tris-Cl solution within a 50-ml polypropylene centrifuge tube, forming a sucrose density gradient. The sucrose gradient with brain homogenate was centrifuged at 100,000 *g* at 4°C for 45 min. Myelin debris was carefully collected from the interface between the sucrose densities, whereas nonmyelin brain debris was discarded with the tube. Crude myelin was washed in Tris-Cl solution and resuspended in sterile PBS to a concentration of 100 mg/ml. 100 µl of crude myelin was pelleted and resuspended in 200 µl of 50 µM CFSE and then incubated at room temperature for 30 min shielded from light. Following incubation, CFSE-labeled myelin was washed in 100 mM glycine in PBS and resuspended in sterile PBS to a concentration of 100 mg/ml.

Phagocytosis analyses

For phagocytosis assay in isolated mouse microglia cells, 5.0×10^4 freshly isolated *Qk*-iCKO and control microglia were cultured on 50-µg/ml poly-D-lysine–treated glass chamber slides. These microglia were incubated with 100 µg/ml pHrodo Red *E. coli* BioParticles conjugate (Life Technologies) for 1 h at 37°C according to the manufacturer's instructions, after which the microglia were washed in sterile PBS and then fixed with 4% PFA in PBS for 15 min at room temperature. After being washed

with sterile PBS, the microglia were immobilized in Vector-Shield mounting media with DAPI counterstaining (H-1500; Vector Laboratories). IF images were directly taken with a DMI8 inverted fluorescent microscope without any further staining. Alternatively, these microglia were incubated with 1 mg/ml of the isolated myelin debris for 3 h at 37°C. Chamber slides were fixed with 4% PFA, washed with PBS to remove residual myelin debris, and blocked with 10% goat serum. Then the cells were stained with anti-Mbp antibody overnight at 4°C and incubated with secondary antibodies conjugated with AlexaFluor 594 for 45 min at room temperature. VECTASHIELD with DAPI was used to mount the coverslips. IF images were taken with a DMI8 inverted fluorescent microscope. The fluorescence intensity within microglia was calculated using ImageJ software for further quantitative analyses.

Phagocytosis assay was also performed in EOC 20 and RAW 264.7 cell lines. EOC 20 and RAW 264.7 cells were cultured in their respective growth medium for 24 h, either on poly-D-lysine–treated glass coverslips within a 12-well plate at a density of 4.0×10^4 cells per well or in an eight-chamber glass slide at a density of 1.0×10^4 per chamber. For the pHrodo Red *E. coli* BioParticles conjugate phagocytosis assay, the conjugate was added to all wells of EOC 20 and RAW 264.7 cells to a final concentration of 100 µg/ml according to the manufacturer's instructions. Simultaneously with the addition of the conjugate, SSO, a Cd36 inhibitor, was coadministered to the treatment wells to a final concentration of 25 µM or 50 µM, whereas DMSO was added as control. The cells were subsequently incubated at 37°C for 1 h, after which the adherent cells were washed in sterile PBS and then fixed with 4% PFA in PBS for 15 min at room temperature. Cells were further washed with sterile PBS and immobilized in VECTASHIELD mounting media with DAPI counterstaining before imaging with fluorescent microscopy. For CFSE-labeled myelin phagocytosis, preprepared CFSE-labeled myelin was added to all wells of EOC 20 and RAW 264.7 cells to a final concentration of 1.0 mg/ml. Simultaneously with the addition of the labeled myelin, SSO was coadministered to the treatment wells to a final concentration of 25 µM or 50 µM, whereas DMSO was added as control. The cells were subsequently incubated at 37°C for 3.5 h, after which adherent cells were washed in sterile PBS and then fixed with 4% PFA in PBS for 15 min at room temperature. After fixation, cells were washed with sterile PBS and immobilized in VECTASHIELD mounting media with DAPI counterstaining before imaging with fluorescent microscopy.

Determination of demyelination and remyelination

To determine demyelination and remyelination, we studied the central part of the CC, which is the large tract of white matter that exhibits the greatest and most consistent pathological changes in the CPZ-induced demyelinating model. The myelin in the CC was analyzed with Mbp staining as described previously (Praet et al., 2014; Skripuletz et al., 2013). Demyelination and remyelination were evaluated by measuring the percentage of Mbp-positive area relative to the total area of the CC using ImageJ software. Demyelination and remyelination were also evaluated with TEM to quantify the percentage of myelinated axons relative to the total number of axons in the CC. In addition, the g-ratio, axon density, and axonal diameter were also quantified during the remyelination process.

Human specimens

Fresh-frozen tissue specimens were obtained from the Rocky Mountain MS Center Tissue Bank and stored at −80°C until use. In total, eight postmortem brain slices, including four control brain slices from donors without neurological disease and four brain slices from patients with primary progressive MS, were analyzed. The patients' ages at the time of death, pathological diagnosis, postmortem interval, sex, cause of death, disease duration, and disease-modifying therapies are shown in Table S1. Lesions were recognized grossly, dissected, and embedded in optimal cutting temperature compound. 20-µm-thick frozen sections were sliced and stored at −80°C until use. Histological verification of primary progressive MS lesions followed the Lassmann/Brück method (Kuhlmann et al., 2017). The active rim of lesions was characterized by microglial activation and T cell infiltration (Popescu et al., 2013), as indicated by IF staining of $IBA1^+$ and $CD3^+$ cells. This area was used for subsequent analyses. The frontal lobe white matter from neurological disease-free human brains was used as control tissue. The expression of QKI in microglia was evaluated by costaining of QKI and IBA1. IF images were taken using a DMI8 inverted fluorescent microscope, and three fields of view were taken at 200× magnification for each sample. The intensities of QKI in all of the $IBA1^+$ cells were quantified in an area of 0.3 mm^2 using ImageJ software and used for further quantification.

Statistics

Statistical tests performed in this study included two-tailed unpaired Student's *t* test for two-group comparison, one-way or two-way ANOVA followed by Tukey's post hoc test and χ^2 test, as indicated in the figure legends. Data are presented as mean ± SD (SD). All analyses were performed using Prism software (version 7; GraphPad). Levels of significance are indicated by asterisks (*, $P < 0.05$; **, $P < 0.01$; ***, $P < 0.001$; ****, $P < 0.0001$), and P values <0.05 were considered statistically significant in all cases. For CPZ diet–induced demyelination and remyelination, representative data from three independent experiments are shown. The number of animals in each experiment is indicated in the figure legends. For phagocytosis assay and RIP-qPCR, representative data from at least three independent experiments are shown. There were no randomization or blinding events during the experiments.

Study approval

All mice were maintained in a C57BL/6 background in pathogen-free conditions at the facility of The University of Texas MD Anderson Cancer Center. All animal studies were performed with the approval of the Institutional Animal Care and Use Committee of The University of Texas MD Anderson Cancer Center.

Fresh-frozen human tissue specimens were obtained from the Rocky Mountain MS Center Tissue Bank. Informed consent and ethical approval for the use of human samples were

collected by the Rocky Mountain MS Center Tissue Bank. The institutional review board of the Human Research Protection Program of The University of Texas MD Anderson Cancer Center provided guidelines for human tissue study procedures (PA16-0803).

Online supplemental material

Fig. S1 demonstrates that Qki in microglia is induced by demyelination in the CNS and depletion of Qki does not impair microgliosis in response to CPZ-induced demyelination. Fig. S2 shows that loss of one copy of the *Cx3cr1* allele does not impact microglial phagocytosis and the response to CPZ-induced demyelination in *Cx3cr1*$^{CreER\text{-}EYFP+/-}$ mice. Fig. S3 shows that the expression of Qki in Gfap$^+$ astrocyte and Olig2$^+$ oligodendrocyte lineage cells was not affected in *Qk*-iCKO mice and shows axonal damage indicated by synaptophysin in 6-wk CPZ-treated mice. Fig. S4 demonstrates that depletion of Qki in microglia impaired alternative splicing of genes involved in phagocytic activity. Fig. S5 shows that Qki was knocked down by ON-TARGETplus siRNA reagents (three individual siRNAs) in stable cells and Qki-5 was reintroduced by treatment of doxycycline. Table S1 summarizes information on patients whose brain samples were used in this study. Table S2 shows a complete list of the differentially spliced events by depletion of Qki in microglia isolated from the CC of 8-wk-old *Qk*-iCKO mice and control mice injected with tamoxifen followed by 6-wk administration of the CPZ diet. Table S3 lists the sequences of the primers used in this study.

Acknowledgments

We thank Shan Jiang, Chythra R. Chandregowda, and Kun Zhao for mouse husbandry and care and all members of the Hu laboratory for helpful discussions. We thank Rocio Isabel Zorrilla-Veloz for her assistance on the graphical abstract. We thank Yuan Qi for performing alternative splicing analyses. We thank Kenneth Dunner Jr. for electron microscopy studies. We especially thank Dr. David M. Wildrick for his editorial assistance. We thank Dr. John R. Corboy and Caroline Miller (Rocky Mountain MS Center Tissue Bank, University of Colorado, Aurora, CO) for providing human brain specimens from the Rocky Mountain MS Center Tissue Bank, University of Colorado.

This study was supported by the National Institutes of Health/National Cancer Institute under Cancer Center Support Grant P30CA016672. This investigation was supported in part by a grant from the National Multiple Sclerosis Society and a Cancer Prevention and Research Institute of Texas grant (RP120348 and RP170002). J. Hu is supported by grants from the National Cancer Institute (R37CA214800), American Cancer Society (RSG-17-029-01-CSM), Sontag Foundation, Brockman Foundation, and by an MD Anderson Internal Research Grant. A.B. Heimberger is supported by National Institutes of Health R01 grant CA120813.

Author contributions: J. Ren, X. Zhou, and J. Hu designed the study and wrote the manuscript. J. Ren and C. Dai performed the experiments. J.A. Barnes contributed to the RIP assay and phagocytosis assay. X. Chen, T. Shingu, and L. Yuan assisted in collection of samples and mouse work. A.B. Heimberger provided some experimental materials and contributed to the interpretation of data. Y. Wang and Y. Chen performed the bioinformatics analyses.

Disclosures: A.B. Heimberger reported personal fees from Celldex Therapeutics, Caris Life Science, WCG Clinical, and DNAtrix; grants from Merck, and "other" from Moleculin and Carthera outside the submitted work. No other disclosures were reported.

Submitted: 22 February 2019
Revised: 7 August 2019
Accepted: 3 September 2020

References

Åberg, K., P. Saetre, E. Lindholm, B. Ekholm, U. Pettersson, R. Adolfsson, and E. Jazin. 2006. Human QKI, a new candidate gene for schizophrenia involved in myelination. *Am. J. Med. Genet. B. Neuropsychiatr. Genet.* 141B: 84–90. https://doi.org/10.1002/ajmg.b.30243

Aguzzi, A., B.A. Barres, and M.L. Bennett. 2013. Microglia: scapegoat, saboteur, or something else? *Science*. 339:156–161. https://doi.org/10.1126/science.1227901

Ajami, B., J.L. Bennett, C. Krieger, W. Tetzlaff, and F.M. Rossi. 2007. Local self-renewal can sustain CNS microglia maintenance and function throughout adult life. *Nat. Neurosci.* 10:1538–1543. https://doi.org/10.1038/nn2014

Arandjelovic, S., and K.S. Ravichandran. 2015. Phagocytosis of apoptotic cells in homeostasis. *Nat. Immunol.* 16:907–917. https://doi.org/10.1038/ni.3253

Bhasin, M., M. Wu, and S.E. Tsirka. 2007. Modulation of microglial/macrophage activation by macrophage inhibitory factor (TKP) or tuftsin (TKPR) attenuates the disease course of experimental autoimmune encephalomyelitis. *BMC Immunol.* 8:10. https://doi.org/10.1186/1471-2172-8-10

Cantuti-Castelvetri, L., D. Fitzner, M. Bosch-Queralt, M.T. Weil, M. Su, P. Sen, T. Ruhwedel, M. Mitkovski, G. Trendelenburg, D. Lütjohann, et al. 2018. Defective cholesterol clearance limits remyelination in the aged central nervous system. *Science*. 359:684–688. https://doi.org/10.1126/science.aan4183

Chen, Y., D. Tian, L. Ku, D.J. Osterhout, and Y. Feng. 2007. The selective RNA-binding protein quaking I (QKI) is necessary and sufficient for promoting oligodendroglia differentiation. *J. Biol. Chem.* 282:23553–23560. https://doi.org/10.1074/jbc.M702045200

Chen, A.J., J.H. Paik, H. Zhang, S.A. Shukla, R. Mortensen, J. Hu, H. Ying, B. Hu, J. Hurt, N. Farny, et al. 2012. STAR RNA-binding protein Quaking suppresses cancer via stabilization of specific miRNA. *Genes Dev.* 26: 1459–1472. https://doi.org/10.1101/gad.189001.112

Chénard, C.A., and S. Richard. 2008. New implications for the QUAKING RNA binding protein in human disease. *J. Neurosci. Res.* 86:233–242. https://doi.org/10.1002/jnr.21485

Colonna, M., and O. Butovsky. 2017. Microglia Function in the Central Nervous System During Health and Neurodegeneration. *Annu. Rev. Immunol.* 35:441–468. https://doi.org/10.1146/annurev-immunol-051116-052358

Conn, S.J., K.A. Pillman, J. Toubia, V.M. Conn, M. Salmanidis, C.A. Phillips, S. Roslan, A.W. Schreiber, P.A. Gregory, and G.J. Goodall. 2015. The RNA binding protein quaking regulates formation of circRNAs. *Cell*. 160: 1125–1134. https://doi.org/10.1016/j.cell.2015.02.014

Darbelli, L., and S. Richard. 2016. Emerging functions of the Quaking RNA-binding proteins and link to human diseases. *Wiley Interdiscip. Rev. RNA*. 7:399–412. https://doi.org/10.1002/wrna.1344

de Bruin, R.G., L. Shiue, J. Prins, H.C. de Boer, A. Singh, W.S. Fagg, J.M. van Gils, J.M. Duijs, S. Katzman, A.O. Kraaijeveld, et al. 2016. Quaking promotes monocyte differentiation into pro-atherogenic macrophages by controlling pre-mRNA splicing and gene expression. *Nat. Commun.* 7: 10846. https://doi.org/10.1038/ncomms10846

Fu, H., G. Yang, M. Wei, L. Liu, L. Jin, X. Lu, L. Wang, L. Shen, J. Zhang, H. Lu, et al. 2012. The RNA-binding protein QKI5 is a direct target of C/EBPα and delays macrophage differentiation. *Mol. Biol. Cell*. 23:1628–1635. https://doi.org/10.1091/mbc.e11-05-0412

Fu, R., Q. Shen, P. Xu, J.J. Luo, and Y. Tang. 2014. Phagocytosis of microglia in the central nervous system diseases. *Mol. Neurobiol.* 49:1422–1434. https://doi.org/10.1007/s12035-013-8620-6

Fujimoto, T., Y. Ohsaki, M. Suzuki, and J. Cheng. 2013. Imaging lipid droplets by electron microscopy. *Methods Cell Biol.* 116:227–251. https://doi.org/10.1016/B978-0-12-408051-5.00012-7

Galarneau, A., and S. Richard. 2005. Target RNA motif and target mRNAs of the Quaking STAR protein. *Nat. Struct. Mol. Biol.* 12:691–698. https://doi.org/10.1038/nsmb963

Gao, Z., and S.E. Tsirka. 2011. Animal Models of MS Reveal Multiple Roles of Microglia in Disease Pathogenesis. *Neurol. Res. Int.* 2011. 383087. https://doi.org/10.1155/2011/383087

Gudi, V., S. Gingele, T. Skripuletz, and M. Stangel. 2014. Glial response during cuprizone-induced de- and remyelination in the CNS: lessons learned. *Front. Cell. Neurosci.* 8:73. https://doi.org/10.3389/fncel.2014.00073

Han, M.H., D.H. Lundgren, S. Jaiswal, M. Chao, K.L. Graham, C.S. Garris, R.C. Axtell, P.P. Ho, C.B. Lock, J.I. Woodard, et al. 2012. Janus-like opposing roles of CD47 in autoimmune brain inflammation in humans and mice. *J. Exp. Med.* 209:1325–1334. https://doi.org/10.1084/jem.20101974

Han, J., M. Wang, M. Ren, and H. Lou. 2017. Contributions of triggering-receptor-expressed-on-myeloid-cells-2 to neurological diseases. *Int. J. Neurosci.* 127:368–375. https://doi.org/10.1080/00207454.2016.1264072

Heppner, F.L., M. Greter, D. Marino, J. Falsig, G. Raivich, N. Hövelmeyer, A. Waisman, T. Rülicke, M. Prinz, J. Priller, et al. 2005. Experimental autoimmune encephalomyelitis repressed by microglial paralysis. *Nat. Med.* 11:146–152. https://doi.org/10.1038/nm1177

Hu, J., A.L. Ho, L. Yuan, B. Hu, S. Hua, S.S. Hwang, J. Zhang, T. Hu, H. Zheng, B. Gan, et al. 2013. From the Cover: Neutralization of terminal differentiation in gliomagenesis. *Proc. Natl. Acad. Sci. USA.* 110:14520–14527. https://doi.org/10.1073/pnas.1308610110

Janda, E., L. Boi, and A.R. Carta. 2018. Microglial Phagocytosis and Its Regulation: A Therapeutic Target in Parkinson's Disease? *Front. Mol. Neurosci.* 11:144. https://doi.org/10.3389/fnmol.2018.00144

Kondo, A., T. Nakano, and K. Suzuki. 1987. Blood-brain barrier permeability to horseradish peroxidase in twitcher and cuprizone-intoxicated mice. *Brain Res.* 425:186–190. https://doi.org/10.1016/0006-8993(87)90499-9

Krasemann, S., C. Madore, R. Cialic, C. Baufeld, N. Calcagno, R. El Fatimy, L. Beckers, E. O'Loughlin, Y. Xu, Z. Fanek, et al. 2017. The TREM2-APOE Pathway Drives the Transcriptional Phenotype of Dysfunctional Microglia in Neurodegenerative Diseases. *Immunity.* 47:566–581.e9. https://doi.org/10.1016/j.immuni.2017.08.008

Kuda, O., T.A. Pietka, Z. Demianova, E. Kudova, J. Cvacka, J. Kopecky, and N.A. Abumrad. 2013. Sulfo-N-succinimidyl oleate (SSO) inhibits fatty acid uptake and signaling for intracellular calcium via binding CD36 lysine 164: SSO also inhibits oxidized low density lipoprotein uptake by macrophages. *J. Biol. Chem.* 288:15547–15555. https://doi.org/10.1074/jbc.M113.473298

Kuhlmann, T., S. Ludwin, A. Prat, J. Antel, W. Brück, and H. Lassmann. 2017. An updated histological classification system for multiple sclerosis lesions. *Acta Neuropathol.* 133:13–24. https://doi.org/10.1007/s00401-016-1653-y

Lampron, A., A. Larochelle, N. Laflamme, P. Préfontaine, M.M. Plante, M.G. Sánchez, V.W. Yong, P.K. Stys, M.E. Tremblay, and S. Rivest. 2015. Inefficient clearance of myelin debris by microglia impairs remyelinating processes. *J. Exp. Med.* 212:481–495. https://doi.org/10.1084/jem.20141656

Larocque, D., J. Pilotte, T. Chen, F. Cloutier, B. Massie, L. Pedraza, R. Couture, P. Lasko, G. Almazan, and S. Richard. 2002. Nuclear retention of MBP mRNAs in the quaking viable mice. *Neuron.* 36:815–829. https://doi.org/10.1016/S0896-6273(02)01055-3

Lenz, K.M., and L.H. Nelson. 2018. Microglia and Beyond: Innate Immune Cells As Regulators of Brain Development and Behavioral Function. *Front. Immunol.* 9:698. https://doi.org/10.3389/fimmu.2018.00698

Li, Q., and B.A. Barres. 2018. Microglia and macrophages in brain homeostasis and disease. *Nat. Rev. Immunol.* 18:225–242. https://doi.org/10.1038/nri.2017.125

Li, Z., Y. Zhang, D. Li, and Y. Feng. 2000. Destabilization and mislocalization of myelin basic protein mRNAs in quaking dysmyelination lacking the QKI RNA-binding proteins. *J. Neurosci.* 20:4944–4953. https://doi.org/10.1523/JNEUROSCI.20-13-04944.2000

Linehan, E., Y. Dombrowski, R. Snoddy, P.G. Fallon, A. Kissenpfennig, and D.C. Fitzgerald. 2014. Aging impairs peritoneal but not bone marrow-derived macrophage phagocytosis. *Aging Cell.* 13:699–708. https://doi.org/10.1111/acel.12223

Liu, J., D. Tian, M. Murugan, U.B. Eyo, C.F. Dreyfus, W. Wang, and L.J. Wu. 2015. Microglial Hv1 proton channel promotes cuprizone-induced demyelination through oxidative damage. *J. Neurochem.* 135:347–356. https://doi.org/10.1111/jnc.13242

Luo, C., C. Jian, Y. Liao, Q. Huang, Y. Wu, X. Liu, D. Zou, and Y. Wu. 2017. The role of microglia in multiple sclerosis. *Neuropsychiatr. Dis. Treat.* 13:1661–1667. https://doi.org/10.2147/NDT.S140634

Marschallinger, J., T. Iram, M. Zardeneta, S.E. Lee, B. Lehallier, M.S. Haney, J.V. Pluvinage, V. Mathur, O. Hahn, D.W. Morgens, et al. 2020. Lipid-droplet-accumulating microglia represent a dysfunctional and proinflammatory state in the aging brain. *Nat. Neurosci.* 23:194–208. https://doi.org/10.1038/s41593-019-0566-1

Matsushima, G.K., and P. Morell. 2001. The neurotoxicant, cuprizone, as a model to study demyelination and remyelination in the central nervous system. *Brain Pathol.* 11:107–116. https://doi.org/10.1111/j.1750-3639.2001.tb00385.x

Meerbrey, K.L., G. Hu, J.D. Kessler, K. Roarty, M.Z. Li, J.E. Fang, J.I. Herschkowitz, A.E. Burrows, A. Ciccia, T. Sun, et al. 2011. The pINDUCER lentiviral toolkit for inducible RNA interference in vitro and in vivo. *Proc. Natl. Acad. Sci. USA.* 108:3665–3670. https://doi.org/10.1073/pnas.1019736108

Mildner, A., H. Schmidt, M. Nitsche, D. Merkler, U.K. Hanisch, M. Mack, M. Heikenwalder, W. Brück, J. Priller, and M. Prinz. 2007. Microglia in the adult brain arise from Ly-6ChiCCR2+ monocytes only under defined host conditions. *Nat. Neurosci.* 10:1544–1553. https://doi.org/10.1038/nn2015

Miron, V.E., T. Kuhlmann, and J.P. Antel. 2011. Cells of the oligodendroglial lineage, myelination, and remyelination. *Biochim. Biophys. Acta.* 1812:184–193. https://doi.org/10.1016/j.bbadis.2010.09.010

Muzio, L., G. Martino, and R. Furlan. 2007. Multifaceted aspects of inflammation in multiple sclerosis: the role of microglia. *J. Neuroimmunol.* 191:39–44. https://doi.org/10.1016/j.jneuroim.2007.09.016

Natrajan, M.S., A.G. de la Fuente, A.H. Crawford, E. Linehan, V. Nuñez, K.R. Johnson, T. Wu, D.C. Fitzgerald, M. Ricote, B. Bielekova, et al. 2015. Retinoid X receptor activation reverses age-related deficiencies in myelin debris phagocytosis and remyelination. *Brain.* 138:3581–3597. https://doi.org/10.1093/brain/awv289

Neumann, H., M.R. Kotter, and R.J. Franklin. 2009. Debris clearance by microglia: an essential link between degeneration and regeneration. *Brain.* 132:288–295. https://doi.org/10.1093/brain/awn109

Olah, M., S. Amor, N. Brouwer, J. Vinet, B. Eggen, K. Biber, and H.W. Boddeke. 2012. Identification of a microglia phenotype supportive of remyelination. *Glia.* 60:306–321. https://doi.org/10.1002/glia.21266

Parkhurst, C.N., G. Yang, I. Ninan, J.N. Savas, J.R. Yates, III, J.J. Lafaille, B.L. Hempstead, D.R. Littman, and W.B. Gan. 2013. Microglia promote learning-dependent synapse formation through brain-derived neurotrophic factor. *Cell.* 155:1596–1609. https://doi.org/10.1016/j.cell.2013.11.030

Poliani, P.L., Y. Wang, E. Fontana, M.L. Robinette, Y. Yamanishi, S. Gilfillan, and M. Colonna. 2015. TREM2 sustains microglial expansion during aging and response to demyelination. *J. Clin. Invest.* 125:2161–2170. https://doi.org/10.1172/JCI77983

Popescu, B.F., I. Pirko, and C.F. Lucchinetti. 2013. Pathology of multiple sclerosis: where do we stand? *Continuum (Minneap. Minn.).* 19(4 Multiple Sclerosis):901–921.

Praet, J., C. Guglielmetti, Z. Berneman, A. Van der Linden, and P. Ponsaerts. 2014. Cellular and molecular neuropathology of the cuprizone mouse model: clinical relevance for multiple sclerosis. *Neurosci. Biobehav. Rev.* 47:485–505. https://doi.org/10.1016/j.neubiorev.2014.10.004

Prinz, M., and J. Priller. 2014. Microglia and brain macrophages in the molecular age: from origin to neuropsychiatric disease. *Nat. Rev. Neurosci.* 15:300–312. https://doi.org/10.1038/nrn3722

Raine, C.S., L. Scheinberg, and J.M. Waltz. 1981. Multiple sclerosis. Oligodendrocyte survival and proliferation in an active established lesion. *Lab. Invest.* 45:534–546.

Rolfe, A.J., D.B. Bosco, E.N. Broussard, and Y. Ren. 2017. In Vitro Phagocytosis of Myelin Debris by Bone Marrow-Derived Macrophages. *J. Vis. Exp.* https://doi.org/10.3791/56322

Rosales, C., and E. Uribe-Querol. 2017. Phagocytosis: A Fundamental Process in Immunity. *BioMed Res. Int.* 2017. 9042851. https://doi.org/10.1155/2017/9042851

Sardiello, M., M. Palmieri, A. di Ronza, D.L. Medina, M. Valenza, V.A. Gennarino, C. Di Malta, F. Donaudy, V. Embrione, R.S. Polishchuk, et al. 2009. A gene network regulating lysosomal biogenesis and function. *Science.* 325:473–477. https://doi.org/10.1126/science.1174447

Sarlus, H., and M.T. Heneka. 2017. Microglia in Alzheimer's disease. *J. Clin. Invest*. 127:3240–3249. https://doi.org/10.1172/JCI90606

Settembre, C., A. Fraldi, D.L. Medina, and A. Ballabio. 2013. Signals from the lysosome: a control centre for cellular clearance and energy metabolism. *Nat. Rev. Mol. Cell Biol*. 14:283–296. https://doi.org/10.1038/nrm3565

Shingu, T., A.L. Ho, L. Yuan, X. Zhou, C. Dai, S. Zheng, Q. Wang, Y. Zhong, Q. Chang, J.W. Horner, et al. 2017. Qki deficiency maintains stemness of glioma stem cells in suboptimal environment by downregulating endolysosomal degradation. *Nat. Genet*. 49:75–86. https://doi.org/10.1038/ng.3711

Sidman, R.L., M.M. Dickie, and S.H. Appel. 1964. Mutant Mice (Quaking and Jimpy) with Deficient Myelination in the Central Nervous System. *Science*. 144:309–311. https://doi.org/10.1126/science.144.3616.309

Sidman, R.L., B. Kosaras, B.M. Misra, and S.L. Senft. 1999. High Resolution Mouse Brain Atlas. http://www.hms.harvard.edu/research/brain

Skripuletz, T., D. Hackstette, K. Bauer, V. Gudi, R. Pul, E. Voss, K. Berger, M. Kipp, W. Baumgärtner, and M. Stangel. 2013. Astrocytes regulate myelin clearance through recruitment of microglia during cuprizone-induced demyelination. *Brain*. 136:147–167. https://doi.org/10.1093/brain/aws262

Underhill, D.M., and H.S. Goodridge. 2012. Information processing during phagocytosis. *Nat. Rev. Immunol*. 12:492–502. https://doi.org/10.1038/nri3244

Uribe-Querol, E., and C. Rosales. 2017. Control of Phagocytosis by Microbial Pathogens. *Front. Immunol*. 8:1368. https://doi.org/10.3389/fimmu.2017.01368

Wake, H., A.J. Moorhouse, and J. Nabekura. 2011. Functions of microglia in the central nervous system--beyond the immune response. *Neuron Glia Biol*. 7:47–53. https://doi.org/10.1017/S1740925X12000063

Wang, S., J. Zan, M. Wu, W. Zhao, Z. Li, Y. Pan, Z. Sun, and J. Zhu. 2015. miR-29a promotes scavenger receptor A expression by targeting QKI (quaking) during monocyte-macrophage differentiation. *Biochem. Biophys. Res. Commun*. 464:1–6. https://doi.org/10.1016/j.bbrc.2015.05.019

Yamanaka, M., T. Ishikawa, A. Griep, D. Axt, M.P. Kummer, and M.T. Heneka. 2012. PPARγ/RXRα-induced and CD36-mediated microglial amyloid-β phagocytosis results in cognitive improvement in amyloid precursor protein/presenilin 1 mice. *J. Neurosci*. 32:17321–17331. https://doi.org/10.1523/JNEUROSCI.1569-12.2012

Zhou, X., C. He, J. Ren, C. Dai, S.R. Stevens, Q. Wang, D. Zamler, T. Shingu, L. Yuan, C.R. Chandregowda, et al. 2020. Mature myelin maintenance requires Qki to coactivate PPARβ-RXRα-mediated lipid metabolism. *J. Clin. Invest*. 130:2220–2236. https://doi.org/10.1172/JCI131800

JEM

Supplemental material

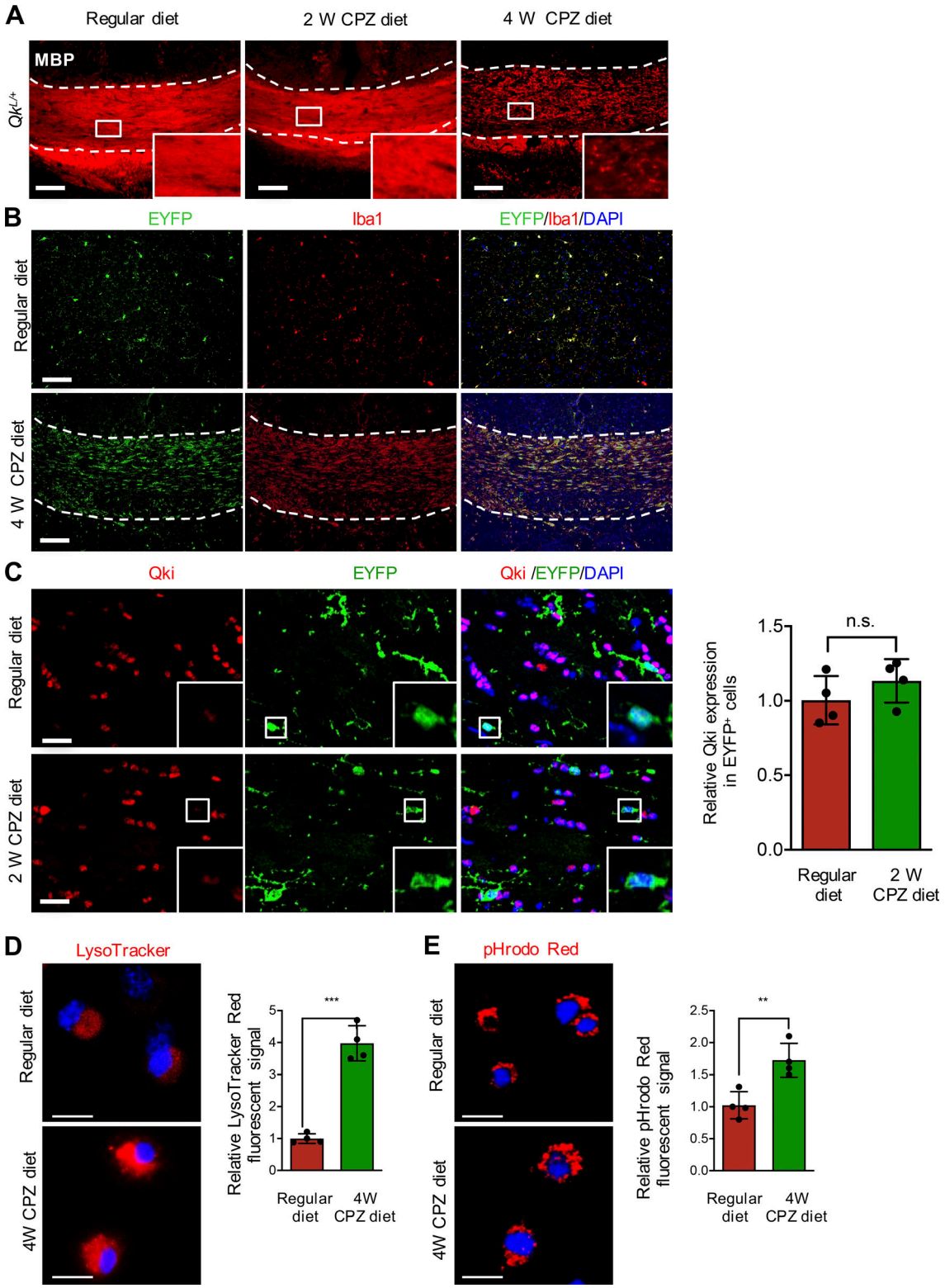

Figure S1. **Qki in microglia is induced by demyelination in the CNS. (A)** Representative images of IF of Mbp in the CCs of 8-wk-old control mice with 2- or 4-wk administration of the CPZ diet or the regular diet (n = 4 mice/group). **(B)** Representative images of IF of EYFP and Iba1 in the cortex of 8-wk-old *Cx3cr1*$^{CreER\text{-}EYFP}$ mice receiving the regular diet (top panels) or the CCs of 8-wk-old *Cx3cr1*$^{CreER\text{-}EYFP}$ receiving the CPZ diet (bottom panels) for 4 wk (n = 4/group). The regions between the dashed lines indicate the CC. **(C)** Representative images of IF and quantification of Qki and EYFP in the CCs of 8-wk-old control mice receiving the regular diet or the CPZ diet for 2 wk (n = 4/group). **(D and E)** Representative images and quantification of LysoTracker Red (D) and pHrodo Red (E) in microglia isolated as described in C and treated with LysoTracker Red or pHrodo Red as indicated. Scale bars: 100 µm in A and B, 50 µm in C, and 20 µm in D and E. Data are means ± SD. Statistics were calculated using unpaired two-tailed Student's t test (D and F). **, P < 0.01; ***, P < 0.001. Data represent three independent experiments (D and E). n.s., not significant; W, week.

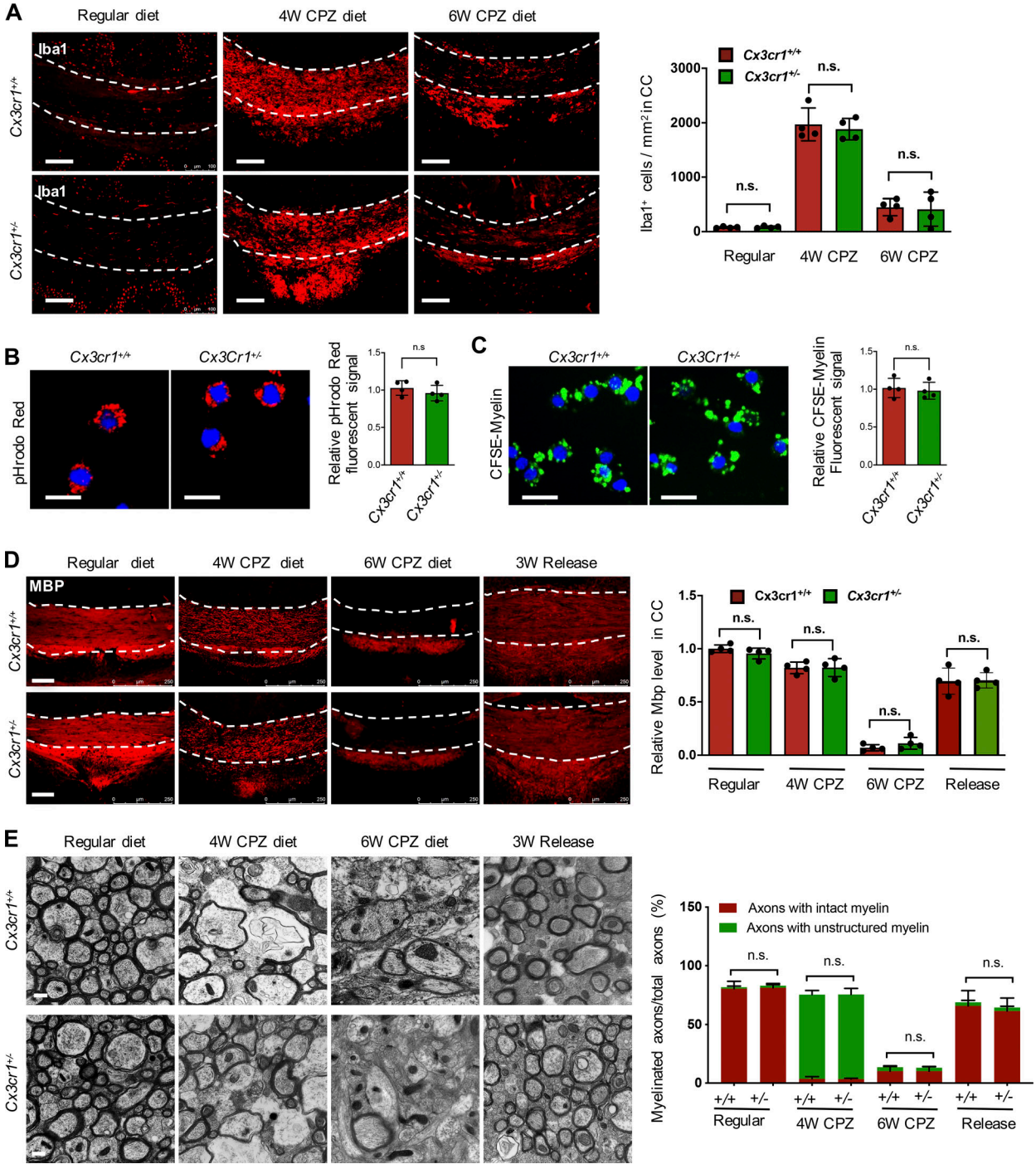

Figure S2. **The heterogeneous deletion of *Cx3cr1* in microglia does not affect its proliferation and phagocytic activity and the demyelinating and remyelinating courses of the CPZ-induced demyelination model. (A)** Representative images of IF and quantification of Iba1 in the CCs of 8-wk-old *Cx3cr1*$^{+/+}$ and *Cx3cr1*$^{+/-}$ mice with 4- or 6-wk administration of the CPZ diet or the regular diet (n = 4 mice/group). Scale bars: 100 µm. **(B and C)** Representative images and quantification of pHrodo Red (B) and CFSE-labeled myelin (C) in microglia isolated from the CCs of 8-wk-old *Cx3cr1*$^{+/+}$ and *Cx3cr1*$^{+/-}$ mice with 4-wk administration of the CPZ diet and incubated with pHrodo Red and CFSE-labeled myelin as indicated. Scale bars: 20 µm. **(D)** Representative images of IF and quantification of Mbp in the CCs of 8-wk-old *Cx3cr1*$^{+/+}$ and *Cx3cr1*$^{+/-}$ mice administered the regular diet, the CPZ diet for 4 wk, the CPZ diet for 6 wk, or the CPZ diet for 6 wk followed by the normal diet for 3 wk. Scale bars: 100 µm. **(E)** Representative electron micrographs and quantification in the CCs of 8-wk-old *Cx3cr1*$^{+/+}$ and *Cx3cr1*$^{+/-}$ mice administered the regular diet, the CPZ diet for 4 wk, the CPZ diet for 6 wk, or the CPZ diet for 6 wk followed by the normal diet for 3 wk (n = 4 mice/group). Scale bars: 2 µm. Data are means ± SD. Statistics were calculated using two-way ANOVA with Tukey's post hoc tests (A and D), unpaired two-tailed Student's t test (B and C), and χ^2 test (E). Data represent three independent experiments (B and C). The regions between the dashed lines indicate the CC (A and D). n.s., not significant; W, week.

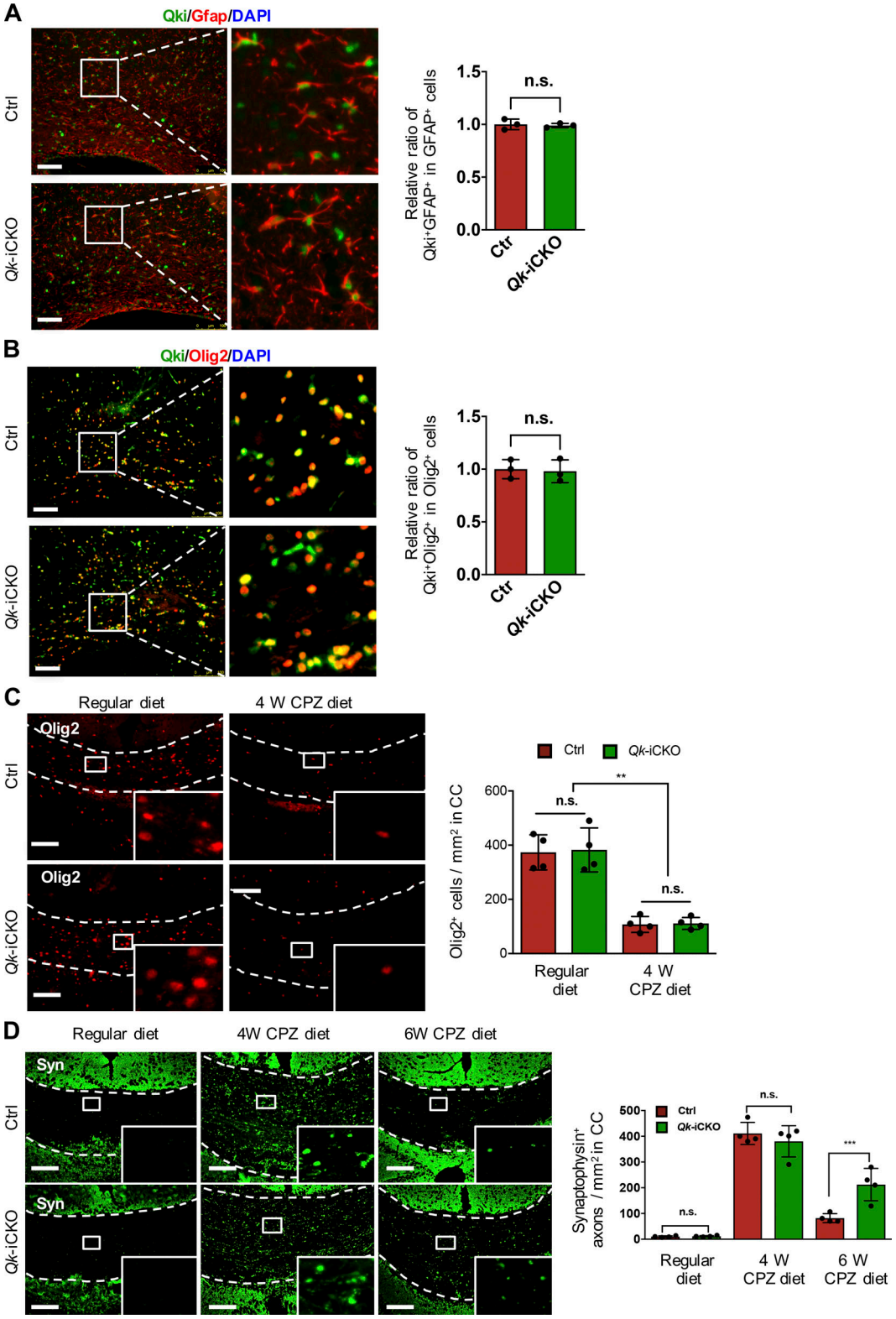

Figure S3. **Depletion of Qki in microglia does not affect the expression of Qki in astrocytes and oligodendrocytes and CPZ-induced myelin damage. (A and B)** Representative images of IF of Qki-Gfap (A) and Qki-Olig2 (B) in the CCs of *Qk*-iCKO mice and control (Ctrl) mice 1 wk after tamoxifen injection at P14. **(C)** Representative images of IF and quantification of oligodendrocyte lineage cells (Olig2-positive) in the CCs of 8-wk-old *Qk*-iCKO and control mice with tamoxifen injection followed by 4 wk of the CPZ diet or the regular diet. **(D)** Representative images of IF and quantification of synaptophysin (Syn) in the CCs of 8-wk-old *Qk*-iCKO and control mice with tamoxifen injection followed by 4- or 6-wk administration of the CPZ diet. *n* = 4 mice/group. Scale bars: 100 µm. Data are means ± SD. Statistics were calculated using unpaired two-tailed Student's *t* test (A and B) and two-way ANOVA with Tukey's post hoc tests (C and D). **, P < 0.01; ***, P < 0.001. The regions between the dashed lines indicate the CC (C and D). n.s., not significant.

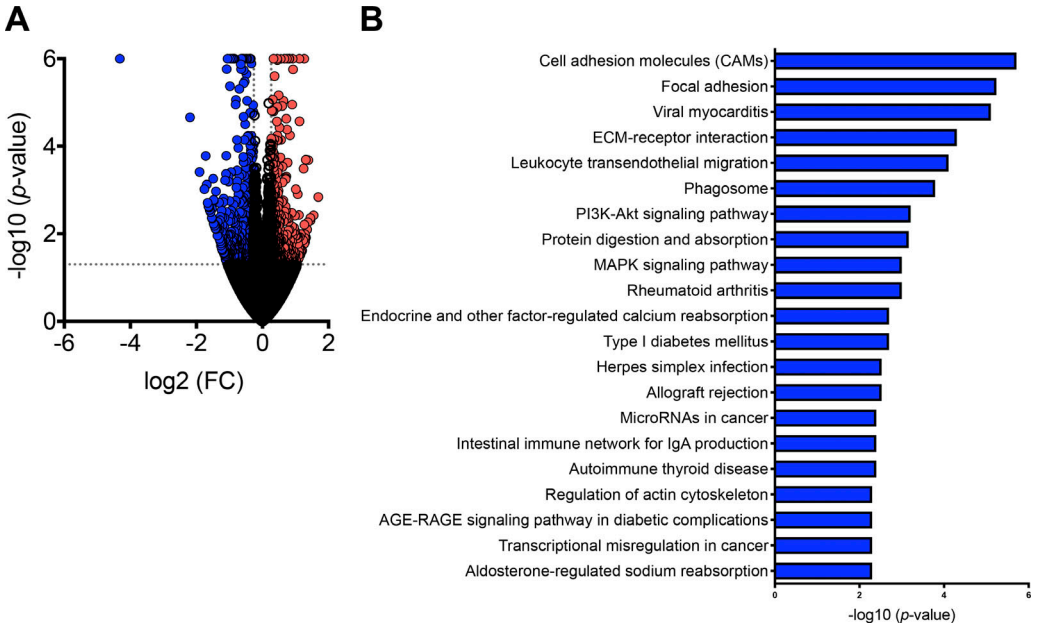

Figure S4. **Depletion of Qki in microglia impaired alternative splicing of the genes involved in phagocytic activity. (A)** Volcano plot showing the differentially expressed genes in microglia isolated from the CC of 8-wk-old *Qk*-iCKO mice and control mice injected with tamoxifen followed by 6-wk administration of the CPZ diet (n = 4/group). Red and blue represent genes whose expression were up-regulated and down-regulated, respectively, upon depletion of Qki. **(B)** Bar graph showing the top 21 enriched pathways based on the differentially spliced events in the samples in A (n = 4 samples/group). ECM, extracellular matrix.

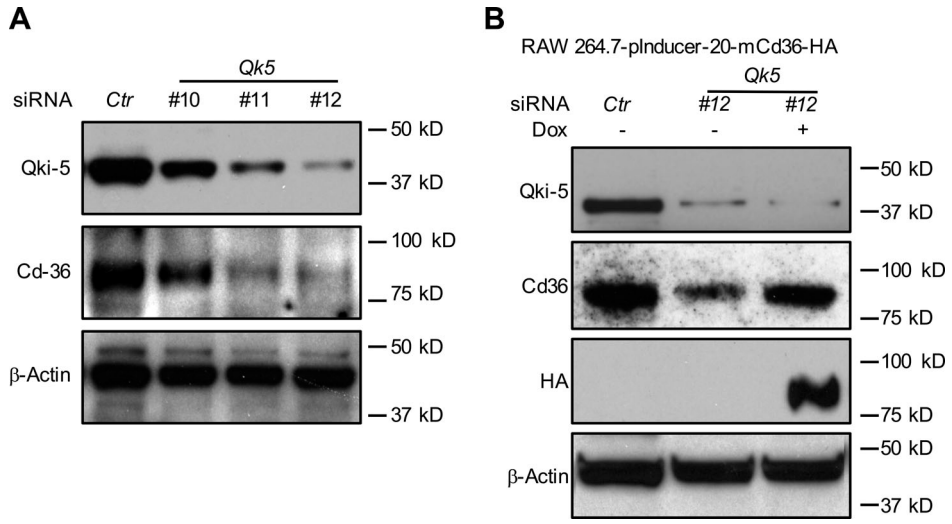

Figure S5. **Cd36 mediates Qki-induced phagocytic activity in RAW 264.7 cells. (A and B)** Stable cell line with ectopic expression of pInducer-20-mCd36-HA was generated in RAW 264.7 cells. **(A)** Qki was knocked down by ON-TARGETplus siRNA reagents (three individual siRNAs) in the stable cells. **(B)** Qki-5 was reintroduced by treatment of doxycycline (Dox). The expression of Qki and Cd36 was determined by Western blot as indicated. β-Actin was used as loading control (Ctr). Data represent three independent experiments.

Tables S1–S3 are provided online. Table S1 shows patients' age at the time of death, pathological diagnosis, postmortem interval, sex, cause of death, disease duration, and disease-modifying therapies. Table S2 presents a complete list of the differentially spliced events by depletion of Qki in microglia isolated from the CC of 8-wk-old *Qk*-iCKO mice and control mice injected with tamoxifen followed by 6-wk administration of the CPZ diet. Table S3 provides a complete list of the sequences of the primers used in this study.